

An efficient cell-centered nodal integral method for multi-dimensional Burgers' equations

Nadeem Ahmed^a, Ram Prakash Bharti^{a,1}, and Suneet Singh^b

^aComplex Fluid Dynamics and Microfluidics (CFDM) Lab, Department of Chemical Engineering, Indian Institute of Technology Roorkee, Roorkee-247667, India

Phone: +91-9410694711

^bDepartment of Energy Science and Engineering, Indian Institute of Technology Bombay, Mumbai-400076, India

Phone: +91-22-2576-7843

Email IDs: 26ahmedansari@gmail.com; suneet.singh@iitb.ac.in; rpbharti@iitr.ac.in

Abstract

An efficient coarse-mesh nodal integral method (NIM), based on cell-centered variables and referred to as cell-centered NIM (CCNIM), is developed and applied for solving multi-dimensional, time-dependent, Burgers' equations. Unlike traditional NIM, which utilizes surface-averaged variables as discrete unknowns, this innovative approach formulates the final expression of the numerical scheme using discrete unknowns represented by cell-centered or node-averaged variables. By relying on these cell centroids, the proposed CCNIM approach presents several advantages compared to traditional NIM. These include a simplified implementation process in terms of local coordinate systems, enhanced flexibility regarding the higher order of accuracy in time, straightforward formulation for higher-degree temporal derivatives, and offering a viable option for coupling with other physics. The multidimensional time-dependent Burgers' problems with known analytical solutions are solved in order to validate the developed scheme. Furthermore, a detailed comparison between the proposed CCNIM approach and other traditional NIM schemes is conducted to showcase its

¹ Corresponding Author

effectiveness. The simplicity and robustness of the approach provide a strong foundation for its seamless extension to more complex fluid flow problems.

Keywords: *Burgers' equations; Difference equations; Analytical nodal methods; Coarse-mesh methods; Cell-centered nodal integral method*

Nomenclature

a	Half of the node size in the x -direction
b	Half of the node size in the y -direction
Re	Reynolds number
\bar{S}	Pseudo-source term
\bar{u}^{xy}	x and y -space averaged velocity in the t -direction
\bar{u}^{xt}	x -space and time-averaged velocity in the y -direction
\bar{u}^{yt}	y -space and time-averaged velocity in the x -direction
\bar{u}^0	Approximation of the convective velocity in the x -direction at current timestep
\bar{v}^{xy}	x and y -space averaged velocity in the t -direction
\bar{v}^{xt}	x -space and time-averaged velocity in the y -direction
\bar{v}^{yt}	y -space and time-averaged velocity in the x -direction
\bar{v}^0	Approximation of the convective velocity in the y -direction at current timestep

Greek symbols

Δt	Time step
Δx	Node size in the x -direction
Δy	Node size in the y -direction
τ	Half of the time step

Superscripts and subscripts

i	Spatial index in the x -direction
j	Spatial index in the y -direction
k	Temporal index
x	Transverse averaging in the x -direction
y	Transverse averaging in the y -direction
t	Transverse averaging in time

Abbreviations

CCNIM	Cell-centered nodal integral method
NIMs	Nodal integral methods
MCCNIM	Modified cell-centered nodal integral methods
ODEs	Ordinary differential equations
PDEs	Partial differential equations

1 Introduction

Over the past few decades, numerous nodal schemes have been developed to address complex partial differential equations (PDEs) in scientific and engineering applications [1–7]. These methods are specifically designed to handle the challenges associated with large-scale computations, such as extensive memory requirements and high computational expense [5,7]. One of the main advantages of nodal schemes is their ability to produce numerical solutions with accuracy comparable to that of more conventional approaches, but in significantly less computational time [5]. This efficiency is largely achieved by using a coarser mesh size, which reduces the number of computational elements and, consequently, the overall computational workload. For a given mesh size, a second-order coarse-mesh scheme is likely to result in smaller numerical errors compared to a second-order finite-difference scheme [4]. This is because nodal schemes include the analytical preprocessing (or local analytical solution) within each node in the development procedure [8]. This makes them particularly useful for large-scale problems where computational resources are limited, or where quick turnaround times are critical.

Various approaches to nodal methods have been explored in the literature to solve the neutron diffusion equation [1–13]. Some of these approaches formulate the final discretized scheme in terms of surface-averaged variables [11,12], while others are based on node-averaged variables [8,9,13]. In the nuclear industry, both methods have proven to be highly accurate and efficient, sharing a common primary step known as the Transverse Integration Procedure (TIP). TIP simplifies PDEs at each node by transforming them into a system of ordinary differential equations (ODEs). The analytical solutions of these transversely averaged ODEs are then computed within each node. Then these analytical solutions are subjected to some physically relevant constraint conditions which results in the final expression of the numerical scheme. The final numerical scheme for the surface-averaged based nodal method includes surface-averaged variables as the discrete unknowns, whereas the node-averaged based scheme uses node-averaged variables as the discrete unknowns. Both schemes have been successfully

applied in the nuclear industry and are effective at solving PDEs efficiently. The surface-averaged based nodal methods have successfully extended their applications to fluid flow problems, and popularly known as the Nodal Integral Method (NIM) [11,14–16]. However, nodal schemes based on node-averaged variables have been less popular in fluid flow community, primarily due to the complexities involved in their development process [9,13]. Recently, advancements in nodal schemes utilizing node-averaged variables for fluid flow problems have emerged, collectively termed the "cell-centered nodal integral method" (CCNIM). This terminology aligns with the conventions in the fluid flow community, where "node-averaged" is often referred to as "cell-centered."

Shober et al. [9] are credited with being the first to develop the CCNIM for solving the neutron diffusion equation. Additionally, Shober thesis [13] provides a comprehensive discussion of the CCNIM method, which builds upon the initial step of the widely used TIP, as discussed earlier, a common feature in various nodal methodologies. However, CCNIM deviates significantly from the standard procedure in traditional NIM, which is to use surface-averaged variables at the border surface of the node as boundary conditions. As boundary conditions for the solution of these ODEs, CCNIM uses interface-averaged flow and interface-averaged variables from neighbouring nodes rather than surface-averaged variables. This modification results in a formulation that is based on cell-centered variables at each node, as opposed to the well-known surface-averaged variables per node within traditional NIMs. The temporal derivative is treated explicitly in the initial development of CCNIM, which offers certain benefits over conventional NIM. These include a straightforward formulation for higher-degree temporal derivatives, improved flexibility with respect to the higher level of accuracy in time, a simplified implementation procedure in terms of local coordinate systems, and a promising alternative for coupling with other physics. A detailed explanation of these advantages is available in the earlier work on CCNIM [17–19]. Due to explicit treatment of temporal derivative, the final system produced by CCNIM links algebraic equations with ODEs, creating a complicated system known as a system of differential-algebraic equations (DAEs). DAEs present considerable challenges in terms of complexity, largely stemming from the intricate coupling between their algebraic and differential components, along with other contributing factors. Furthermore, CCNIM has been hindered by challenges like managing Neumann boundary conditions and not being applicable to one-dimensional problems. Consequently, a modified version of CCNIM known as MCCNIM is created in order to address the issues of CCNIM. MCCNIM discretizes both space and time in the nodal framework, ensuring second-

order accuracy in both dimensions. This approach eliminates the need for complex DAE systems, significantly simplifying the computational process by generating an algebraic set of equations for the discrete unknowns at each node. Furthermore, the use of a straightforward flux definition facilitates the seamless incorporation of Neumann boundary conditions. MCCNIM is also adaptable to one-dimensional problems. Notably, by treating the temporal derivative explicitly, the same MCCNIM framework, along with its flux definition, can be readily converted into a CCNIM method.

Until now, both the schemes, CCNIM and MCCNIM, have been exclusively developed for solving linear fluid flow problems, such as heat conduction and linear convection-diffusion equations. In this work, we extend MCCNIM to tackle nonlinear partial differential equations, specifically Burgers' equations. It is worth noting that we chose to develop MCCNIM because it can be applied to both one- and two-dimensional problems, whereas CCNIM is limited to two-dimensional problems. However, if necessary, the CCNIM approach could also be developed by taking the temporal derivative outside and following a development procedure similar to that outlined in the present work for MCCNIM. To validate the proposed scheme, we solve various one- and two-dimensional Burgers' problems with available analytical solutions. Additionally, a comprehensive comparison of the proposed scheme with previously published results is presented to demonstrate its effectiveness. The rate of convergence is rigorously tested for multiple problems, confirming that the scheme achieves second-order accuracy in both space and time.

The paper is structured as follows: Sections 2 and 3 develop the MCCNIM for solving one- and two-dimensional time-dependent Burgers' equations. Numerical results in Section 4 showcase the performance of the scheme, and the conclusions and discussions are provided in Section 5.

2 Formalism

The essential steps of the MCCNIM are briefly outlined here, with a detailed discussion of their application to one- and two-dimensional Burgers' equations provided in the following sections. Issues related to handling nonlinear convective velocity in both one- and two-dimensional cases are addressed in the concluding section.

In general, there are six significant stages in the MCCNIM implementation procedure.

1. Finite-sized rectangular elements, known as nodes or cells, are used to divide the space-time domain. The width of each cell is equal to $2a_i$, denoted as Δx . Similarly, the height of each cell is equal to $2\tau_j$, denoted as Δt . This may be seen in Panel (b) of Figure 1. After discretization, the Transverse Integration Process (TIP) is applied to each cell, transforming the partial differential equations (PDEs) into a group of ordinary differential equations (ODEs).
2. The set of ODEs is separated into homogeneous and inhomogeneous components. The homogeneous part, which is easily integrable, is placed on the left side of the differential equation. Conversely, the inhomogeneous part, which is not readily integrable, is placed on the right side and is known as the pseudo-source term. These pseudo-source terms are expanded to a specific order using Legendre polynomials. Subsequently within each cell, the homogeneous components are solved analytically with the surface-averaged heat flux and interface variable acting as boundary conditions.
3. The analytical solutions of these ODEs are then integrated (averaged) along the remaining direction to derive the expression of the cell-centered (node-averaged) variables.
4. By ensuring that the continuity criteria are satisfied at the shared boundary of neighbouring nodes, we obtain equations for variables that are averaged over the surface.
5. Following that, physically relevant constraint conditions are established in order to close the system of equations. The initial two constraint conditions are obtained through systematic manipulation of the definitions of pseudo-source terms from Step 2 and the utilization of surface-averaged variable expressions from Step 4. This process establishes linkages between surface-averaged variables and pseudo-source terms. A supplementary constraint condition is derived by calculating the average of the original PDEs over each dimension.
6. At last, the final set of algebraic equations in terms of cell-centered (node-averaged) variables is derived by incorporating the expressions of the surface-averaged variables obtained in step 4 into the constraint conditions.

The steps discussed for MCCNIM are further elaborated by applying them to the one- and two-dimensional time-dependent Burgers' equations in the following subsections. We used the one-dimensional transient Burgers' equation to provide a detailed formulation of our proposed

approach for addressing a nonlinear problem. Following a similar procedure, a brief derivation of the two-dimensional Burgers' equation is also presented in the subsequent section.

2.1 One-dimensional Burgers' equation

The one-dimensional time-dependent Burgers' equation is given as

$$\frac{\partial u(x,t)}{\partial t} + u(x,t) \frac{\partial u(x,t)}{\partial x} = \frac{1}{Re} \frac{\partial^2 u(x,t)}{\partial x^2} \quad (1)$$

where $u(x,t)$ is the velocity, and Re is the Reynolds number. As shown in panel (a) of Figure 1, the space-time domain for the one-dimensional problem described by Eq. (1) is discretized into rectangular nodes indexed by i and j , where i represents the spatial index and j the temporal index. Each node (i,j) is defined by dimensions $(\Delta x \times \Delta t)$, with the width of each cell equal to $2a_i$ (i.e., $\Delta x = 2a_i$) and the height equal to $2\tau_j$ (i.e., $\Delta t = 2\tau_j$). The origin of the node is positioned at the node center, as illustrated in panel (b) of Figure 1.

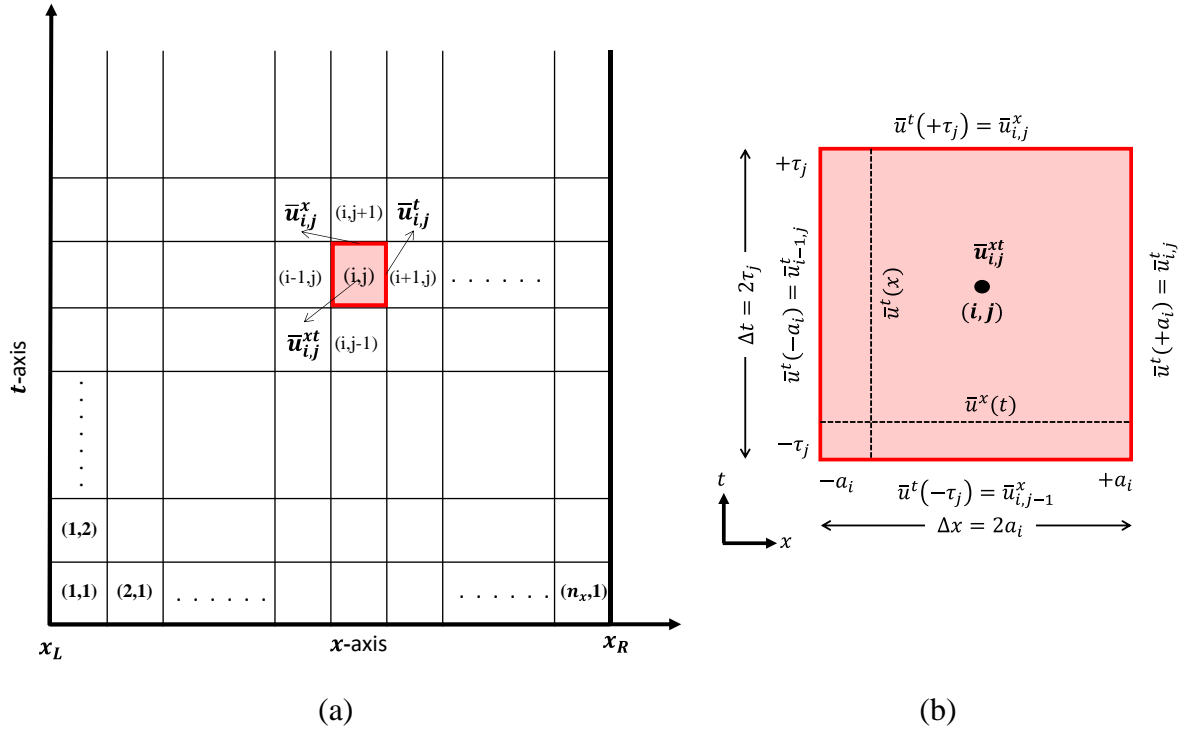


Figure 1 (a) A schematic representation of the global (x, t) space, and its division into the rectangular nodes or elements for one-dimensional transient problems in MCCNIM. (b) Local coordinate system and transverse-averaged quantities within the node (i, j) .

Prior to the development of the numerical scheme, the one-dimensional Burgers' equation given by Eq. (1) are reformulated in terms of the local coordinate system, as shown below:

$$\frac{\partial u(x,t)}{\partial t} + \bar{u}^0 \frac{\partial u(x,t)}{\partial x} = \frac{1}{Re} \frac{\partial^2 u(x,t)}{\partial x^2} \quad (2)$$

where \bar{u}^0 is the node-averaged u velocity at the previous time step. The definition of \bar{u}^0 is discussed in Section 2.1.7.

2.1.1 Transverse integration process

This step, known as the transverse integration procedure (TIP), is common to all nodal schemes in which, after discretizing the space-time domain, the PDE is integrated transversely (averaged) in each direction. Since we are developing the scheme for the one-dimensional Burgers' equation given by Eq. (1), which involves both x and t directions, the integration is performed sequentially. First, the integration is performed in the x -direction using the operator $\frac{1}{2a_i} \int_{-a_i}^{+a_i} dx$ in Eq. (1), followed by the t -direction using the operator $\frac{1}{2\tau_j} \int_{-\tau_j}^{+\tau_j} dt$ in Eq. (1) over each node (i, j) of the discretized domain.

Employing the operator $\frac{1}{2a_i} \int_{-a_i}^{+a_i} dx$ on Eq. (1) yields

$$\frac{1}{2a_i} \int_{-a_i}^{+a_i} \left(\frac{\partial u(x,t)}{\partial t} \right) dx = \frac{1}{2a_i} \int_{-a_i}^{+a_i} \left(\frac{1}{Re} \frac{\partial^2 u(x,t)}{\partial x^2} - \bar{u}^0 \frac{\partial u(x,t)}{\partial x} \right) dx \quad (3)$$

Note that Eq. (3) is arranged so that the terms requiring straightforward integration are placed on the left-hand side (L.H.S.), while the remaining terms are shifted to the right-hand side to serve as pseudo-source terms. The first ODE which is averaged in space and dependent on time for node (i, j) is then given as

$$\frac{d\bar{u}^x(t)}{dt} = \bar{S}_1^x(t) \quad (4)$$

Likewise, implementing the operator $\frac{1}{2\tau_j} \int_{-\tau_j}^{+\tau_j} dt$ on Eq. (1) and adhering to the analogous methodology, an additional time-averaged and space-dependent ODE can be obtained as

$$\frac{1}{Re} \frac{d^2 \bar{u}^t(x)}{dx^2} - \bar{u}^0 \frac{d\bar{u}^t(x)}{dx} = \bar{S}_2^t(x) \quad (5)$$

where transverse-averaged physical quantities ($\bar{u}^t(x)$, $\bar{u}^x(t)$) and pseudo-source terms ($\bar{S}_1^x(t)$ and $\bar{S}_2^t(x)$) are defined as

$$\bar{u}^t(x) = \frac{1}{2\tau_j} \int_{-\tau_j}^{+\tau_j} u(x, t) dt, \quad (6)$$

$$\bar{u}^x(t) = \frac{1}{2a_i} \int_{-a_i}^{+a_i} u(x,t) dx, \quad (7)$$

$$\bar{S}_1^x(t) = \frac{1}{2a_i} \int_{-a_i}^{+a_i} \left(\frac{1}{Re} \frac{\partial^2 u(x,t)}{\partial x^2} - \bar{u}^0 \frac{\partial u(x,t)}{\partial x} \right) dx, \quad (8)$$

$$\bar{S}_2^t(x) = \frac{1}{2\tau_j} \int_{-\tau_j}^{+\tau_j} \frac{\partial u(x,t)}{\partial t} dt. \quad (9)$$

The product of the averages has been used to estimate the average of the product, representing a second-order approximation. The aforementioned progression holds true for all cells. One crucial step in solving locally transverse-integrated ODEs is to use Legendre polynomials to expand the pseudo-source terms $\bar{S}_1^x(t)$ in Eq. (4), and $\bar{S}_2^t(x)$ in Eq. (5). The expansion of these pseudo-source terms is truncated to the zeroth order during this operation, resulting in a constant. Prior studies have established that by truncating the expansion at the zeroth order level, one can obtain a scheme that is accurate to the second order [11,20,21]. Nevertheless, it is important to acknowledge, that higher-order schemes are possible as a result of choosing to truncate the expansion at higher orders. Following truncation, Eq. (4) and Eq. (5) simplify into two ordinary differential equations (ODEs):

$$\frac{d\bar{u}^x(t)}{dt} = \bar{S}_{1i,j}^{xt}, \quad (10)$$

$$\frac{1}{Re} \frac{d^2 \bar{u}^t(x)}{dx^2} - \bar{u}_{i,j}^0 \frac{d\bar{u}^t(x)}{dx} = \bar{S}_{2i,j}^{xt}. \quad (11)$$

The nodal index is represented by the subscript (i,j) in $\bar{S}_{1i,j}^{xt}$ and $\bar{S}_{2i,j}^{xt}$, where the numerical values 1 and 2 are merely employed for distinguishing the two terms.

2.1.2 Analytical solution of ODEs

The analytical solutions to the ODEs derived in the previous subsection is then implemented within individual nodes. While the first ODE (Eq. (10)) is solved analytically in a manner similar to the traditional NIM, the second ODE (Eq. (11)) is computed using a different approach. This approach involves applying modified cell boundary conditions, in contrast to the conventional NIM [22,23]. Specifically, this method uses both the averaged velocity variable and the averaged heat flux as boundary conditions, as illustrated in Figure 2.

By solving Eq. (10) (first ODE) analytically and applying the nodal boundary condition $\bar{u}^x(t) = \bar{u}^x(+\tau_j)$ at the surface $t = +\tau_j$, as depicted in the panel (a) of Figure 2, we obtain:

$$\bar{u}^x(t) = \bar{S}_{1i,j}^{xt}(t - \tau_j) + \bar{u}^x(+\tau_j). \quad (12)$$

Eq. (12) can be rewritten in (i, j) indexing using $\bar{u}^x(+\tau_j) = \bar{u}_{i,j}^x$ as,

$$\bar{u}^x(t) = \bar{S}_{1i,j}^{xt}(t - \tau_j) + \bar{u}_{i,j}^x. \quad (13)$$

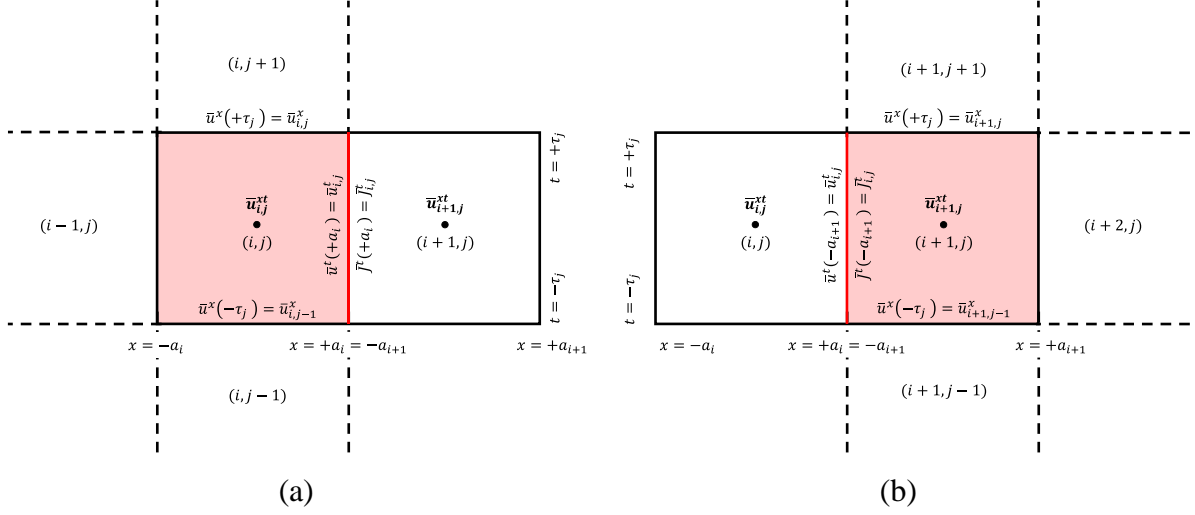


Figure 2 Local boundary conditions for MCCNIM. (a) For node (i, j) . (b) For node $(i + 1, j)$.

The current approach employs the identical analytical solution procedure as the prior CCNIM, however with a simpler definition of interface flux for the boundary conditions. The convective term was incorporated into the definition of flux in the previous CCNIM [18]. The incorporation of the convective term in the flux definition presented a challenge in the previous study when attempting to apply Neumann or insulated boundary conditions with the nodal spirit. Consequently, the insulated boundary conditions were applied using a second-order finite difference approximation, which compromises the fundamental nature of the nodal scheme. To address this issue and enhance the system's adaptability and adherence to physical principles, a straightforward definition of flux was introduced in previous work [17], as illustrated in Figure 2. This revised formulation effectively distinguished between the convective and diffusive aspects of the flux, facilitated the independent application of distinct boundary conditions to each component. Consequently, this enhances the method's practicality and accuracy in simulations. The modified flux at the common edge of the neighbouring nodes is defined as

$$\bar{f}^t(x) = \frac{1}{2\tau_j} \int_{-\tau_j}^{+\tau_j} \frac{\partial u(x,t)}{\partial x} dt = \frac{d\bar{u}^t(x)}{dx} \quad (14)$$

By using the surface-averaged flux defined in Eq. (14) and the surface-averaged velocity as local boundary conditions at the interface between nodes (i, j) and $(i + 1, j)$, as shown in panel (a) of Figure 2, we obtain the solution to the second ODE described by Eq. (11). For node (i, j) , the analytical solution of Eq. (11) is obtained by applying the average velocity $\bar{u}^t(x) = \bar{u}^t(+a_i)$ and averaged flux $\bar{J}^t(x) = \bar{J}^t(+a_i)$ at the interface $x = +a_i$, as depicted in panel (a) of Figure 2, leading to:

$$[\bar{u}^t(x)]_{i,j} = \bar{u}^t(+a_i) - \frac{1 - e^{-Re\bar{u}_{i,j}^0(x-a_i)}}{Re\bar{u}_{i,j}^0} \bar{J}^t(+a_i) - \frac{\left(1 - e^{-Re\bar{u}_{i,j}^0(x-a_i)} + Re\bar{u}_{i,j}^0(x-a_i)\right)}{Re(\bar{u}_{i,j}^0)^2} \bar{S}_{2i,j}^{xt} \quad (15)$$

Similarly, the solution at node $(i + 1, j)$ can be derived using boundary conditions at $x = -a_{i+1}$, $\bar{u}^t(x) = \bar{u}^t(-a_{i+1})$ and $\bar{J}^t(x) = \bar{J}^t(-a_{i+1})$, as depicted in panel (b) of Figure 2, given as follows:

$$[\bar{u}^t(x)]_{i+1,j} = \bar{u}^t(-a_{i+1}) - \frac{1 - e^{-Re\bar{u}_{i+1,j}^0(x+a_{i+1})}}{Re\bar{u}_{i+1,j}^0} \bar{J}^t(-a_{i+1}) - \frac{\left(1 - e^{-Re\bar{u}_{i+1,j}^0(x+a_{i+1})} + Re\bar{u}_{i+1,j}^0(x+a_{i+1})\right)}{Re(\bar{u}_{i+1,j}^0)^2} \bar{S}_{2i+1,j}^{xt} \quad (16)$$

Up to this point, the procedure has strictly adhered to conventional NIM practices. However, a key distinction arises in the boundary conditions for solving Eq. (11). In conventional NIM, surface-averaged variables at both cell edges are used. In contrast, MCCNIM employs both surface-averaged variables and heat fluxes at the interface between adjacent nodes, as shown in Figure 2. A detailed comparison between these approaches was provided in the initial CCNIM paper [17–19].

2.1.3 Evaluation of the cell-centered variable

The solutions derived in the previous subsection for $\bar{u}^x(t)$ given by Eq. (13) and $\bar{u}^t(x)$ given by Eq. (15) and Eq. (16) are now subjected to a second averaging (integration) process to determine the cell-centered variables. Initially, by applying the operator $\frac{1}{2\tau_j} \int_{-\tau_j}^{+\tau_j} dt$ defined in Eq.(13) we obtain:

$$\bar{u}_{i,j}^{xt} = -\tau_j \bar{S}_{1i,j}^{xt} + \bar{u}_{i,j}^x \quad (17)$$

where $\bar{u}_{i,j}^{xt}$ represents the cell-centered (node-averaged) velocity. Note that the pseudo-source term $\bar{S}_{1i,j}^{xt}$ is inherently a cell-centered value following truncation. Now, by applying the operator $\frac{1}{2a_i} \int_{-a_i}^{+a_i} dx$ in Eq. (15) and $\frac{1}{2a_{i+1}} \int_{-a_{i+1}}^{+a_{i+1}} dx$ to Eq. (16), we obtain:

$$\bar{u}_{i,j}^{xt} = \bar{u}^t(+a_i) + \frac{(1 - e^{-Reu_{i,j} - 2a_i Re \bar{u}_{i,j}^0})}{2a_i Re^2 (\bar{u}_{i,j}^0)^2} \bar{J}^t(+a_i) + \frac{(1 - e^{-Reu_{i,j} + 2a_i Re \bar{u}_{i,j}^0 (-1 + a_i Re \bar{u}_{i,j}^0)})}{2a_i Re^2 (\bar{u}_{i,j}^0)^3} \bar{S}_{2i,j}^{xt} \quad (18)$$

$$\bar{u}_{i+1,j}^{xt} = \bar{u}^t(-a_{i+1}) + \frac{(-1 + e^{Reu_{i+1,j} - 2a_{i+1} Re \bar{u}_{i+1,j}^0})}{2a_{i+1} Re^2 (\bar{u}_{i+1,j}^0)^2} \bar{J}^t(-a_{i+1}) + \frac{(-1 + e^{Reu_{i+1,j} - 2a_{i+1} Re \bar{u}_{i+1,j}^0 (1 + a_{i+1} Re \bar{u}_{i+1,j}^0)})}{2a_{i+1} Re^2 (\bar{u}_{i+1,j}^0)^3} \bar{S}_{2i+1,j}^{xt} \quad (19)$$

In Eq. (18) and Eq. (19), each power of the exponential term is written in terms of the local Reynolds number. For instance, at node (i, j) the local Reynolds number is defined as $Reu_{i,j} = 2a_i Re \bar{u}_{i,j}^{xt}$. Furthermore, Eq. (18) and Eq. (19) can also be rearranged to yield,

$$\bar{J}^t(+a_i) = A_{31} (\bar{u}_{i,j}^{xt} - \bar{u}^t(+a_i)) + A_{32} \bar{S}_{2i,j}^{xt} \quad (20)$$

$$\bar{J}^t(-a_{i+1}) = A_{51,i+1} (\bar{u}_{i+1,j}^{xt} - \bar{u}^t(-a_{i+1})) + A_{52,i+1} \bar{S}_{2i+1,j}^{xt} \quad (21)$$

where A_{31} , A_{32} , A_{51} and A_{52} are the coefficients that are dependent on the parameters a_i , $Reu_{i,j}$, and $\bar{u}_{i,j}^{xt}$. The explicit definitions of these coefficients are detailed in Appendix A.

2.1.4 Continuity conditions

Since the surface-averaged velocity is solely needed as a boundary condition for the solution of the first ODE (i.e., Eq. (10)), it is evident that no continuity conditions are required in the temporal direction. As a result, Eq. (17) can be reformulated with all cell-centered values on one side (i.e., the right-hand side), which is presented as:

$$\bar{u}_{i,j}^x = \bar{u}_{i,j}^{xt} + \tau_j \bar{S}_{1i,j}^{xt} \quad (22)$$

Eq. (22) is applicable to node (i, j) . A corresponding equation for node $(i, j - 1)$ can be obtained through a simple index shift, given as

$$\bar{u}_{i,j-1}^x = \bar{u}_{i,j-1}^{xt} + \tau_{j-1} \bar{S}_{1i,j-1}^{xt} \quad (23)$$

Spatially, two continuity conditions must be imposed: (a) continuity of the surface-averaged velocity at the common edge between adjacent nodes, and (b) continuity of the heat flux at the shared edge between the same neighbouring nodes. The continuity of the surface-averaged velocity between nodes (i, j) and $(i + 1, j)$ can be written as

$$\bar{u}^t(+a_i) = \bar{u}^t(-a_{i+1}) = \bar{u}_{i,j}^t \quad (24)$$

Similarly, the continuity of the surface averaged heat flux between nodes (i, j) and $(i + 1, j)$ can be expressed as

$$\bar{J}^t(+a_i) = \bar{J}^t(-a_{i+1}) = \bar{J}_{i,j}^t \quad (25)$$

On applying the continuity conditions utilizing Eq. (20) and Eq. (21) and solving for the surface averaged velocity, $\bar{u}_{i,j}^t$, we get,

$$\bar{u}_{i,j}^t = \frac{A_{32} \bar{S}_{2i,j}^{xt} - A_{52,i+1} \bar{S}_{2i+1,j}^{xt} + A_{31} \bar{u}_{i,j}^{xt} - A_{51,i+1} \bar{u}_{i+1,j}^{xt}}{A_{31} - A_{51,i+1}} \quad (26)$$

Now, substituting the expression for $\bar{u}_{i,j}^t$ from Eq. (26) into either flux equation (i.e., Eq. (20) and Eq. (21)) yields the same expression for $\bar{J}_{i,j}^t$, conforming that the continuity conditions have been met. The resulting expression of $\bar{J}_{i,j}^t$ is as follows:

$$\bar{J}_{i,j}^t = \frac{-A_{32} A_{51,i+1} \bar{S}_{2i,j}^{xt} + A_{31} A_{52,i+1} \bar{S}_{2i+1,j}^{xt} + A_{31} A_{51,i+1} (\bar{u}_{i+1,j}^{xt} - \bar{u}_{i,j}^{xt})}{A_{31} - A_{51,i+1}} \quad (27)$$

Similarly, by changing the index from (i, j) to $(i - 1, j)$, we can readily write analogous expressions for $\bar{u}_{i-1,j}^t$ and $\bar{J}_{i-1,j}^t$ given by,

$$\bar{u}_{i-1,j}^t = \frac{A_{32,i-1} \bar{S}_{2i-1,j}^{xt} - A_{52} \bar{S}_{2i,j}^{xt} + A_{31,i-1} \bar{u}_{i-1,j}^{xt} - A_{51} \bar{u}_{i,j}^{xt}}{A_{31,i-1} - A_{51}} \quad (28)$$

$$\bar{J}_{i-1,j}^t = \frac{-A_{32,i-1} A_{51} \bar{S}_{2i-1,j}^{xt} + A_{31,i-1} A_{52} \bar{S}_{2i,j}^{xt} + A_{31,i-1} A_{51} (\bar{u}_{i,j}^{xt} - \bar{u}_{i-1,j}^{xt})}{A_{31,i-1} - A_{51}} \quad (29)$$

It is crucial to note that, for each node (i, j) , we have three equations (Eq. (22), Eq. (26) and Eq. (27)) but six unknowns ($\bar{u}_{i,j}^x$, $\bar{u}_{i,j}^t$, $\bar{J}_{i,j}^t$, $\bar{u}_{i,j}^{xt}$, $\bar{S}_{1i,j}^{xt}$ and $\bar{S}_{2i,j}^{xt}$). Given that the scheme must rely

solely on cell-centered values, it becomes necessary to eliminate the surface-averaged terms from the final set of algebraic equations. To achieve this, three additional constraint conditions are required.

2.1.5 Constraint equations

In order to successfully close the system of equations, we define three physically important constraint conditions in this section. Averaging the original PDE across all dimensions while taking the concept of pseudo-source terms into account yields the first constraint condition. Using the definitions of surface-averaged variables and carefully adjusting the pseudo-source terms, we systematically establish our final two constraint conditions. This procedure creates a crucial connection between the surface-averaged terms and the pseudo-sources.

The first constraint equation is obtained by integrating the original Burgers' equation (Eq. (1)) over the node (i, j) using the operator $\frac{1}{4a_i\tau_j} \int_{-a_i}^{+a_i} \int_{-\tau_j}^{+\tau_j} dt dx$. By incorporating the definitions of $\bar{S}_{1i,j}^{xt}$ from Eq. (10) and $\bar{S}_{2i,j}^{xt}$ from Eq. (11), a relationship between $\bar{S}_{1i,j}^{xt}$ and $\bar{S}_{2i,j}^{xt}$ is established, expressed as:

$$\bar{S}_{1i,j}^{xt} = \bar{S}_{2i,j}^{xt} \quad (30)$$

The two additional constraint conditions are a manipulation of the definition of the pseudo-source terms. The second constraint equation is derived by averaging (integrating) Eq. (8) by employing the operator $\frac{1}{2\tau_j} \int_{-\tau_j}^{+\tau_j} dt$, which yields,

$$\bar{S}_{1i,j}^{xt} = \frac{1}{2a_i} \int_{-a_i}^{+a_i} \left(\frac{1}{Re} \frac{d^2 \bar{u}^t(x)}{dx^2} - \bar{u}_{i,j}^0 \frac{d\bar{u}^t(x)}{dx} \right) dx \quad (31)$$

Now, utilizing the definition of flux, $\bar{J}^t(x) = \frac{d\bar{u}^t(x)}{dx}$, and substituting it in Eq. (31), which will modify Eq. (31) as,

$$\bar{S}_{1i,j}^{xt} = \frac{1}{2a_i} \int_{-a_i}^{+a_i} \left(\frac{1}{Re} \frac{d\bar{J}^t(x)}{dx} - \bar{u}_{i,j}^0 \frac{d\bar{u}^t(x)}{dx} \right) dx \quad (32)$$

It is then reformulated in terms of the surface-averaged velocity and flux, leading to the second constraint condition, expressed as:

$$\bar{S}_{1i,j}^{xt} = \frac{\bar{J}_{i,j}^t - \bar{J}_{i-1,j}^t}{2a_i Re} - \bar{u}_{i,j}^0 \frac{\bar{u}_{i,j}^t - \bar{u}_{i-1,j}^t}{2a_i} \quad (33)$$

Likewise, applying the definition of the second pseudo-source term from Eq. (9), the third constraint equation can be derived as follows:

$$\bar{S}_{2i,j}^{xt} = \frac{\bar{u}_{i,j}^x - \bar{u}_{i,j-1}^x}{2\tau_j} \quad (34)$$

The six equations—Eq. (22), Eq. (26), Eq. (27), Eq. (30), Eq. (33) and Eq. (34)—govern six unknowns ($\bar{u}_{i,j}^x$, $\bar{u}_{i,j}^t$, $\bar{J}_{i,j}^t$, $\bar{u}_{i,j}^{xt}$, $\bar{S}_{1i,j}^{xt}$ and $\bar{S}_{2i,j}^{xt}$). By eliminating the surface-averaged terms, the final set of algebraic equations can now be readily derived.

2.1.6 Set of discrete equations

The first algebraic equation is derived by substituting the time-averaged velocity expressions from Eqs. (26) and (28) and the heat flux expressions from Eqs. (27) and (29) into the second constraint equation (Eq. (33)). This leads to:

$$\bar{S}_{1i,j}^{xt} = F_{31}\bar{S}_{2i,j}^{xt} + F_{32}\bar{S}_{2i-1,j}^{xt} + F_{33}\bar{S}_{2i+1,j}^{xt} + F_{34}\bar{u}_{i,j}^{xt} + F_{35}\bar{u}_{i-1,j}^{xt} + F_{36}\bar{u}_{i+1,j}^{xt} \quad (35)$$

Furthermore, substituting the space-averaged velocity expressions from Eqs. (22) and (23) into the third constraint equation (Eq. (34)) yields the second algebraic equation:

$$\bar{S}_{2i,j}^{xt} = \frac{\bar{S}_{1i,j}^{xt} - \bar{S}_{1i,j-1}^{xt}}{2} + \frac{\bar{u}_{i,j}^{xt} - \bar{u}_{i,j-1}^{xt}}{2\tau_j} \quad (36)$$

By substituting the expressions for $\bar{S}_{1i,j}^{xt}$ and $\bar{S}_{2i,j}^{xt}$ from Eqs. (35) and (36) into the first constraint equation (Eq. (30)), the third algebraic equation is obtained:

$$\begin{aligned} \bar{u}_{i,j}^{xt} = & F_{51}\bar{S}_{2i,j}^{xt} + F_{52}\bar{S}_{2i-1,j}^{xt} + F_{53}\bar{S}_{2i+1,j}^{xt} + F_{54}\bar{S}_{1i,j}^{xt} + F_{55}\bar{S}_{1i,j-1}^{xt} + F_{56}\bar{u}_{i,j-1}^{xt} + \\ & F_{57}\bar{u}_{i-1,j}^{xt} + F_{58}\bar{u}_{i+1,j}^{xt} \end{aligned} \quad (37)$$

The coefficients F 's are detailed in Appendix A. . The discrete unknowns for the cell (i, j) include the variables averaged at the cell centers: $\bar{u}_{i,j}^{xt}$, $\bar{S}_{1i,j}^{xt}$, $\bar{S}_{2i,j}^{xt}$.

2.1.7 Derivation of the nonlinear convective velocity

In the context of Burgers' equation, the velocity $u(x, t)$ in the convection term $u(x, t) \frac{\partial u(x, t)}{\partial x}$ of Eq. (1) is an unknown function, which introduces nonlinearity into the equation. As a result, during the implementation of the key steps in the development process, assumptions must be made regarding the approximation of the convective velocity $u(x, t)$ in the convection term. In the modified NIM [14], the approximation of the convective velocity at a node (i, j) , denoted as $\bar{u}_{i,j}^0$, is determined by averaging the surface-averaged velocities at the current time step, as given by:

$$\bar{u}_{i,j}^0 = \frac{\bar{u}_{i,j}^t + \bar{u}_{i-1,j}^t}{2} \quad (38)$$

Within the context of MCCNIM, we adopt the same definition as provided in MNIM given by Eq. (38). However, it is crucial to emphasize that in MCCNIM, the final discretized equation is expressed in terms of cell-centered values. This is a departure from MNIM, where surface-averaged velocities ($\bar{u}_{i,j}^t$ and $\bar{u}_{i-1,j}^t$) are employed for the approximation of the convective velocity. To maintain consistency, if we intend to utilize the same approximation in MCCNIM, it becomes imperative to apply this approximation in terms of cell-centered values. Hence, utilizing Eq. (26) and Eq. (28) from Section 0, which establishes the connection between the surface-averaged values and cell-centered values. We will employ these expressions to derive Eq. (38) in terms of cell-centered values. To achieve this, substituting the expressions from Eq. (26) and Eq. (28) into Eq. (38), we obtain:

$$\bar{u}_{i,j}^0 = F_{71} \bar{S}_{2i-1,j}^{tx} + F_{72} \bar{S}_{2i,j}^{tx} + F_{73} \bar{S}_{2i+1,j}^{tx} + F_{74} \bar{u}_{i-1,j}^{xt} + F_{75} \bar{u}_{i,j}^{xt} + F_{76} \bar{u}_{i+1,j}^{xt} \quad (39)$$

where the coefficients F_7 's are given in Appendix A.

2.1.8 Boundary conditions

In the scheme described in the previous subsection, the discrete unknowns are represented by dependent variables averaged at the center of each cell. This contrasts with the conventional NIM approach, where unknowns are defined on the cell surfaces [23]. Consequently, since boundary conditions are typically specified at the edges or surfaces of the domain, the implementation of Dirichlet and Neumann boundary conditions at boundary nodes in CCNIM schemes exhibits subtle differences compared to their application in standard NIM schemes.

The expressions for the surface-averaged velocity $\bar{u}_{i,j}^t$ from Eq. (26) and the surface-averaged flux $\bar{J}_{i,j}^t$ from Eq. (27) for interior nodes reveal a dependence on the cell-centered velocities $\bar{u}_{i,j}^{xt}$ and $\bar{u}_{i+1,j}^{xt}$ of two adjacent nodes, specifically (i,j) and $(i,j+1)$, as detailed in Section 0. However, this relationship does not apply at boundary nodes because, at the boundaries, there is only one neighbouring node, as depicted in Figure 3 for the right boundary.

As an illustration, the flux $\bar{J}_{n-1,j}^t$ at the right boundary node (n,j) , shown in Figure 3, is influenced by the cell-centered velocities $\bar{u}_{n-1,j}^{xt}$ and $\bar{u}_{n,j}^{xt}$ from the adjacent nodes $(n-1,j)$ and (n,j) . However, at the right boundary surface, where the flux is given by $\bar{J}_{n,j}^t = \bar{J}_R^t$, only the node (n,j) remains, meaning it solely depends on the cell-centered velocity $\bar{u}_{n,j}^{xt}$. A detailed derivation for the right boundary is provided, and the equation for the left boundary node can be derived in an analogous manner.

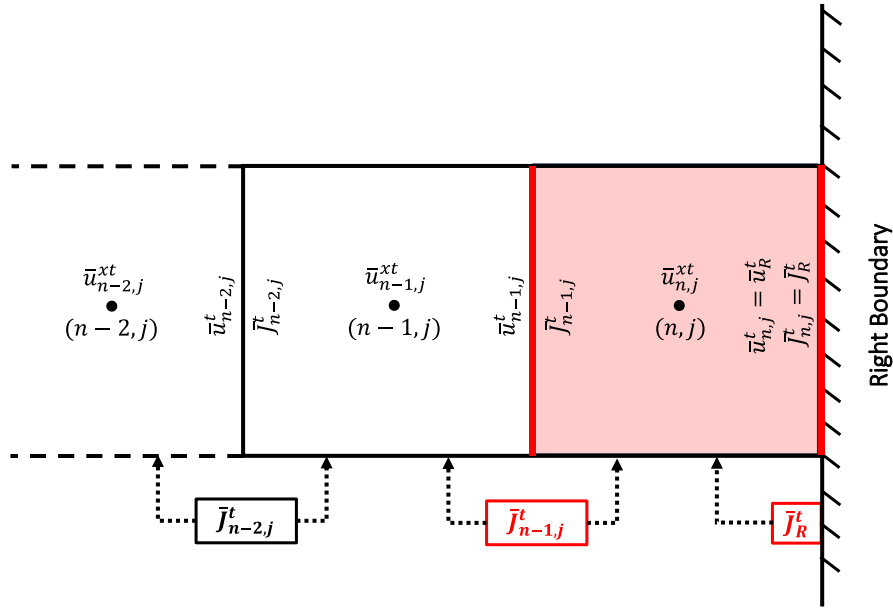


Figure 3 Stencil for right boundary node

2.1.9 Dirichlet boundary conditions

For the right boundary, referring to Eq. (20), $\bar{J}_{i,j}^t$ can be expressed as

$$\bar{J}_{i,j}^t = A_{31}(\bar{u}_{i,j}^{xt} - \bar{u}_{i,j}^t) + A_{32}\bar{S}_{2i,j}^{xt} \quad (40)$$

To simplify the explanation, we define the flux and velocity at the right boundary as \bar{J}_R^t and \bar{u}_R^t , respectively. Using these definitions, Eq. (40) can be reformulated as:

$$\bar{J}_R^t = A_{31}(\bar{u}_{i,j}^{xt} - \bar{u}_R^t) + A_{32}\bar{S}_{2i,j}^{xt} \quad (41)$$

In a similar manner, by applying Eq. (21), the flux equation for the left boundary can be expressed as:

$$\bar{J}_L^t = A_{51}(\bar{u}_{i,j}^{xt} - \bar{u}_L^t) + A_{52}\bar{S}_{2i,j}^{xt} \quad (42)$$

Here, the subscripts “L” and “R” denote the left and right surfaces of the boundary node, respectively. The process for deriving the final set of discrete equations for the right boundary node remains unchanged, except for the second constraint equation (Eq. (33)), which can be written for the right boundary as:

$$\bar{S}_{1i,j}^{xt} = -\frac{\bar{J}_R^t - \bar{J}_{i-1,j}^t}{2a_i} - \bar{u}_{i,j}^0 \frac{\bar{u}_R^t - \bar{u}_{i-1,j}^t}{2a_i} \quad (43)$$

The first algebraic equation can now be derived by substituting the expression for $\bar{u}_{i-1,j}^t$ from Eq. (28), $\bar{J}_{i-1,j}^t$ from Eq. (29), and \bar{J}_R^t from Eq. (41) into the first constraint equation for the right boundary (Eq. (43)). This results in:

$$\bar{S}_{1i,j}^{xt} = F_{31}^R \bar{S}_{2i,j}^{xt} + F_{32}^R \bar{S}_{2i-1,j}^{xt} + F_{34}^R \bar{u}_{i,j}^{xt} + F_{35}^R \bar{u}_{i-1,j}^{xt} + F_{36}^R \bar{u}_R^t \quad (44)$$

It is important to note that the second algebraic equation will be the same for both interior and boundary nodes. By substituting the expressions for $\bar{S}_{2i,j}^{xt}$ from Eq. (35) and $\bar{S}_{1i,j}^{xt}$ from Eq. (44) into the third constraint equation (Eq. (30)), we obtain the third algebraic equation for the right boundary node, which is expressed as:

$$\bar{u}_{i,j}^{xt} = F_{51}^R \bar{S}_{2i,j}^{xt} + F_{52}^R \bar{S}_{2i-1,j}^{xt} + F_{54}^R \bar{S}_{1i,j}^{xt} + F_{55}^R \bar{S}_{1i,j-1}^{xt} + F_{56}^R \bar{u}_{i,j-1}^{xt} + F_{57}^R \bar{u}_{i-1,j}^{xt} + F_{58}^R \bar{u}_R^t \quad (45)$$

The superscript “R” in all the coefficients signifies that they correspond to the right boundary node. The definitions of all the F^R coefficients are provided in Appendix A. The algebraic equations for the left boundary node can be derived using a similar approach.

2.1.10 Neumann boundary conditions

Deriving Neumann boundary conditions in MCCNIM is relatively straightforward. It involves setting the flux, either \bar{J}_L^t or \bar{J}_R^t , to zero or applying the appropriate boundary condition as

required. For instance, if the left boundary is insulated and the right boundary is governed by Dirichlet conditions, \bar{J}_L^t is set to zero, while \bar{J}_R^t is calculated using the corresponding equation (Eq. (41)). Conversely, if the right boundary is insulated and the left boundary follows Dirichlet conditions, \bar{J}_R^t is set to zero, and \bar{J}_L^t is determined from Eq. (42). In cases where both boundaries are insulated, the flux at both surfaces is set to zero. Importantly, the method for obtaining the final set of algebraic equations remains identical to the approach outlined for Dirichlet boundary conditions.

2.2 Two-dimensional coupled Burgers' equations

The two-dimensional time-dependent coupled Burgers' equation is given as

$$\frac{\partial u(x,y,t)}{\partial t} + u(x,y,t) \frac{\partial u(x,y,t)}{\partial x} + v(x,y,t) \frac{\partial u(x,y,t)}{\partial y} = \frac{1}{Re} \left(\frac{\partial^2 u(x,y,t)}{\partial x^2} + \frac{\partial^2 u(x,y,t)}{\partial y^2} \right) + f_x(x,y,t) \quad (46)$$

$$\frac{\partial v(x,y,t)}{\partial t} + u(x,y,t) \frac{\partial v(x,y,t)}{\partial x} + v(x,y,t) \frac{\partial v(x,y,t)}{\partial y} = \frac{1}{Re} \left(\frac{\partial^2 v(x,y,t)}{\partial x^2} + \frac{\partial^2 v(x,y,t)}{\partial y^2} \right) + f_y(x,y,t) \quad (47)$$

The development procedure for two-dimensional Burgers' equation will be the same as that for one-dimensional Burgers' equation derived in Section 2.1. Some essential steps for a two-dimensional case are presented in this section for completeness.

The spatial domain defined by the independent variables (x, y) is divided into nodes of size $\Delta x \times \Delta y$, indexed by i in the x -direction and j in the y -direction. The solution is computed at discrete time intervals of Δt , indexed by k . For transverse integration, each space-time node is assigned dimensions $\Delta x_i = 2a_i$, $\Delta y_j = 2b_j$, and $\Delta t_k = 2\tau_k$, centered at the node. The local coordinate system for the node (i, j, k) is defined by $(-a_i \leq x_i \leq +a_i, -b_j \leq y_j \leq +b_j, -\tau_k \leq t_k \leq +\tau_k)$. Figure 4 illustrates the transverse-averaged quantities on various surfaces, highlighted in different colours, along with the local coordinate system.

Prior to the development of the numerical scheme, the Burgers' equations given by Eq. (46) and Eq. (47) are reformulated in terms of the local coordinate system, as shown below:

$$\frac{\partial u(x,y,t)}{\partial t} + u^0 \frac{\partial u(x,y,t)}{\partial x} + v^0 \frac{\partial u(x,y,t)}{\partial y} = \frac{1}{Re} \left(\frac{\partial^2 u(x,y,t)}{\partial x^2} + \frac{\partial^2 u(x,y,t)}{\partial y^2} \right) + f_x(x,y,t) \quad (48)$$

$$\frac{\partial v(x,y,t)}{\partial t} + u^0 \frac{\partial v(x,y,t)}{\partial x} + v^0 \frac{\partial v(x,y,t)}{\partial y} = \frac{1}{Re} \left(\frac{\partial^2 v(x,y,t)}{\partial x^2} + \frac{\partial^2 v(x,y,t)}{\partial y^2} \right) + f_y(x,y,t) \quad (49)$$

Here u^0 and v^0 represents the node-averaged convective velocities in the x and y -directions, respectively. The definitions of these velocities for the two-dimensional case are provided later in the derivation.

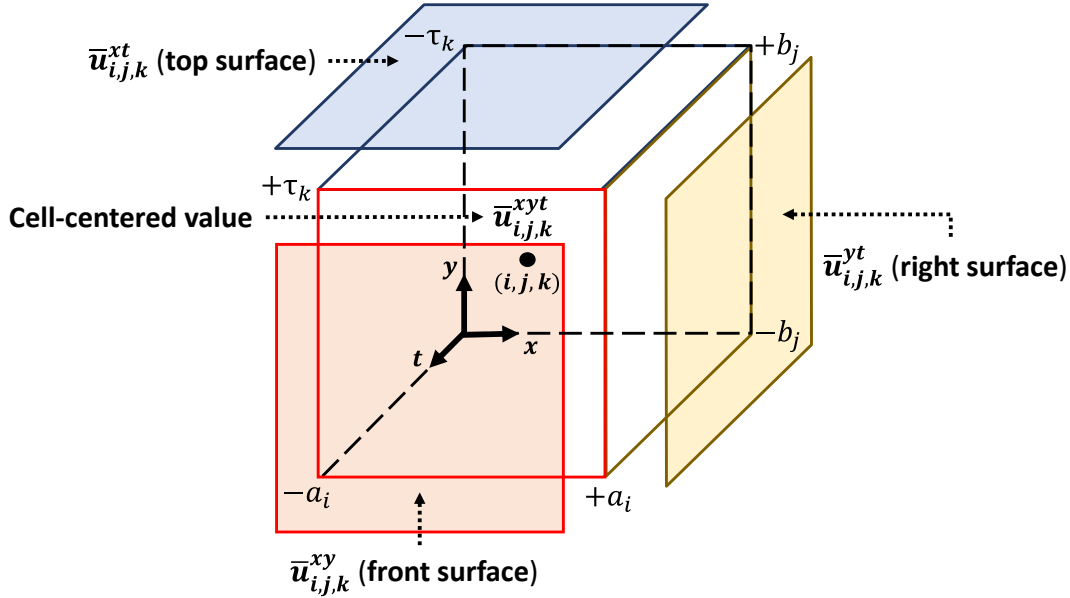


Figure 4 Local coordinate system and transverse-averaged quantities of node (i, j, k) for two-dimensional transient problems in MCCNIM

By performing transverse integration in each direction and truncating the pseudo-source terms to zeroth order, analogous to the one-dimensional case discussed in Section 2.1.1, the resulting set of ODEs for the node (i, j, k) in the context of the two-dimensional Burgers' equations (Eq. (46) and Eq. (47)) is presented as follows:

$$\frac{1}{Re} \frac{d^2 \bar{u}^{yt}(x)}{dx^2} - \bar{u}_{i,j,k}^0 \frac{d\bar{u}^{yt}(x)}{dx} = \bar{S}_{3i,j,k}^{xyt} \quad (50)$$

$$\frac{1}{Re} \frac{d^2 \bar{u}^{xt}(y)}{dy^2} - \bar{v}_{i,j,k}^0 \frac{d\bar{u}^{xt}(y)}{dy} = \bar{S}_{2i,j,k}^{xyt} \quad (51)$$

$$\frac{d\bar{u}^{xy}(t)}{dt} = \bar{S}_{1i,j,k}^{xyt} \quad (52)$$

$$\frac{1}{Re} \frac{d^2 \bar{v}^{yt}(x)}{dx^2} - \bar{u}_{i,j,k}^0 \frac{d\bar{v}^{yt}(x)}{dx} = \bar{S}_{6i,j,k}^{xyt} \quad (53)$$

$$\frac{1}{Re} \frac{d^2 \bar{v}^{xt}(y)}{dy^2} - \bar{v}_{i,j,k}^0 \frac{d\bar{v}^{xt}(y)}{dy} = \bar{S}_{5i,j,k}^{xyt} \quad (54)$$

$$\frac{d\bar{v}^{xy}(t)}{dt} = \bar{S}_{4i,j,k}^{xyt} \quad (55)$$

The three ODEs (Eqs. (50)–(52)) are derived from the x -momentum equation (Eq. (46)), while the subsequent three ODEs (Eqs. (53)–(55)) are obtained from the y -momentum equation (Eq. (47)), both using the process of transverse integration as discussed in 2.1.1. Furthermore, all the assumptions and definitions outlined in Section 2.1 for developing the one-dimensional scheme are equally applicable to the two-dimensional case. The definitions of pseudo-source terms ($\bar{S}_{1i,j,k}^{xyt}$, $\bar{S}_{2i,j,k}^{xyt}$, $\bar{S}_{3i,j,k}^{xyt}$, $\bar{S}_{4i,j,k}^{xyt}$, $\bar{S}_{5i,j,k}^{xyt}$, and $\bar{S}_{6i,j,k}^{xyt}$) are given as

$$\bar{S}_{3i,j,k}^{xyt} = \frac{1}{2\tau_k} \int_{-\tau_k}^{+\tau_k} \frac{d\bar{u}^{xy}(t)}{dt} dt - \frac{1}{2b_j} \int_{-b_j}^{+b_j} \left(\frac{1}{Re} \frac{d^2 \bar{u}^{xt}(y)}{dy^2} - \bar{v}_{i,j,k}^0 \frac{d\bar{u}^{xt}(y)}{dy} \right) dy - \bar{f}_{xi,j,k}^{xyt} \quad (56)$$

$$\bar{S}_{2i,j,k}^{xyt} = \frac{1}{2\tau_k} \int_{-\tau_k}^{+\tau_k} \frac{d\bar{u}^{xy}(t)}{dt} dt - \frac{1}{2a_i} \int_{-a_i}^{+a_i} \left(\frac{1}{Re} \frac{d^2 \bar{u}^{yt}(x)}{dx^2} - \bar{u}_{i,j,k}^0 \frac{d\bar{u}^{yt}(x)}{dx} \right) dx - \bar{f}_{xi,j,k}^{xyt} \quad (57)$$

$$\begin{aligned} \bar{S}_{1i,j,k}^{xyt} = & \frac{1}{2a_i} \int_{-a_i}^{+a_i} \left(\frac{1}{Re} \frac{d^2 \bar{u}^{yt}(x)}{dx^2} - \bar{u}_{i,j,k}^0 \frac{d\bar{u}^{yt}(x)}{dx} \right) dx + \frac{1}{2b_j} \int_{-b_j}^{+b_j} \left(\frac{1}{Re} \frac{d^2 \bar{u}^{xt}(y)}{dy^2} - \right. \\ & \left. \bar{v}_{i,j,k}^0 \frac{d\bar{u}^{xt}(y)}{dy} \right) dy + \bar{f}_{xi,j,k}^{xyt} \end{aligned} \quad (58)$$

$$\bar{S}_{6i,j,k}^{xyt} = \frac{1}{2\tau_k} \int_{-\tau_k}^{+\tau_k} \frac{d\bar{v}^{xy}(t)}{dt} dt - \frac{1}{2b_j} \int_{-b_j}^{+b_j} \left(\frac{1}{Re} \frac{d^2 \bar{v}^{xt}(y)}{dy^2} - \bar{v}_{i,j,k}^0 \frac{d\bar{v}^{xt}(y)}{dy} \right) dy - \bar{f}_{yi,j,k}^{xyt} \quad (59)$$

$$\bar{S}_{5i,j,k}^{xyt} = \frac{1}{2\tau_k} \int_{-\tau_k}^{+\tau_k} \frac{d\bar{v}^{xy}(t)}{dt} dt - \frac{1}{2a_i} \int_{-a_i}^{+a_i} \left(\frac{1}{Re} \frac{d^2 \bar{v}^{yt}(x)}{dx^2} - \bar{u}_{i,j,k}^0 \frac{d\bar{v}^{yt}(x)}{dx} \right) dx - \bar{f}_{yi,j,k}^{xyt} \quad (60)$$

$$\begin{aligned} \bar{S}_{4i,j,k}^{xyt} = & \frac{1}{2a_i} \int_{-a_i}^{+a_i} \left(\frac{1}{Re} \frac{d^2 \bar{v}^{yt}(x)}{dx^2} - \bar{u}_{i,j,k}^0 \frac{d\bar{v}^{yt}(x)}{dx} \right) dx + \frac{1}{2b_j} \int_{-b_j}^{+b_j} \left(\frac{1}{Re} \frac{d^2 \bar{v}^{xt}(y)}{dy^2} - \right. \\ & \left. \bar{v}_{i,j,k}^0 \frac{d\bar{v}^{xt}(y)}{dy} \right) dy + \bar{f}_{yi,j,k}^{xyt} \end{aligned} \quad (61)$$

Notably, the defined pseudo-source terms are already averaged over the entire node and are presented in a manner that facilitates the straightforward derivation of the constraint equations. Upon rearranging the pseudo-source terms, the six constraint equations are formulated in terms of surface-averaged quantities as follows:

$$\bar{S}_{3i,j,k}^{xyt} = \frac{\bar{u}_{i,j,k}^{xy} - \bar{u}_{i,j,k-1}^{xy}}{2\tau_k} + \frac{\bar{J}_{xi,j,k}^{xt} - \bar{J}_{xi,j-1,k}^{xt}}{2b_j Re} + \bar{v}_{i,j,k}^0 \frac{\bar{u}_{i,j,k}^{xt} - \bar{u}_{i,j-1,k}^{xt}}{2b_j} - \bar{f}_{xi,j,k}^{xyt} \quad (62)$$

$$\bar{S}_{2i,j,k}^{xyt} = \frac{\bar{u}_{i,j,k}^{xy} - \bar{u}_{i,j,k-1}^{xy}}{2\tau_k} + \frac{\bar{J}_{xi,j,k}^{yt} - \bar{J}_{xi-1,j,k}^{yt}}{2a_i Re} + \bar{u}_{i,j,k}^0 \frac{\bar{u}_{i,j,k}^{yt} - \bar{u}_{i-1,j,k}^{yt}}{2a_i} - \bar{f}_{xi,j,k}^{xyt} \quad (63)$$

$$\begin{aligned} \bar{S}_{1i,j,k}^{xyt} = & -\frac{\bar{J}_{xi,j,k}^{yt} - \bar{J}_{xi-1,j,k}^{yt}}{2a_i Re} - \bar{u}_{i,j,k}^0 \frac{\bar{u}_{i,j,k}^{yt} - \bar{u}_{i-1,j,k}^{yt}}{2a_i} - \frac{\bar{J}_{xi,j,k}^{xt} - \bar{J}_{xi,j-1,k}^{xt}}{2b_j Re} - \bar{v}_{i,j,k}^0 \frac{\bar{u}_{i,j,k}^{xt} - \bar{u}_{i,j-1,k}^{xt}}{2b_j} + \\ & \bar{f}_{xi,j,k}^{xyt} \end{aligned} \quad (64)$$

$$\bar{S}_{6i,j,k}^{xyt} = \frac{\bar{v}_{i,j,k}^{xy} - \bar{v}_{i,j,k-1}^{xy}}{2\tau_k} + \frac{\bar{J}_{yi,j,k}^{xt} - \bar{J}_{yi,j-1,k}^{xt}}{2b_j Re} + \bar{v}_{i,j,k}^0 \frac{\bar{v}_{i,j,k}^{xt} - \bar{v}_{i,j-1,k}^{xt}}{2b_j} - \bar{f}_{yi,j,k}^{xyt} \quad (65)$$

$$\bar{S}_{5i,j,k}^{xyt} = \frac{\bar{v}_{i,j,k}^{xy} - \bar{v}_{i,j,k-1}^{xy}}{2\tau_k} + \frac{\bar{J}_{yi,j,k}^{yt} - \bar{J}_{yi-1,j,k}^{yt}}{2a_i Re} + \bar{u}_{i,j,k}^0 \frac{\bar{v}_{i,j,k}^{yt} - \bar{v}_{i-1,j,k}^{yt}}{2a_i} - \bar{f}_{yi,j,k}^{xyt} \quad (66)$$

$$\bar{S}_{4i,j,k}^{xyt} = -\frac{\bar{J}_{yi,j,k}^{yt} - \bar{J}_{yi-1,j,k}^{yt}}{2a_i Re} - \bar{u}_{i,j,k}^0 \frac{\bar{v}_{i,j,k}^{yt} - \bar{v}_{i-1,j,k}^{yt}}{2a_i} - \frac{\bar{J}_{yi,j,k}^{xt} - \bar{J}_{yi,j-1,k}^{xt}}{2b_j Re} - \bar{v}_{i,j,k}^0 \frac{\bar{v}_{i,j,k}^{xt} - \bar{v}_{i,j-1,k}^{xt}}{2b_j} + \bar{f}_{yi,j,k}^{xyt} \quad (67)$$

Furthermore, by averaging the original Burgers' equations (i.e., Eq. (46) and Eq. (47)) over the node (i, j, k) using the operator $\frac{1}{8a_i b_j \tau_k} \int_{-a_i}^{+a_i} \int_{-b_j}^{+b_j} \int_{-\tau_k}^{+\tau_k} dt dy dx$ and realising the definition of pseudo source terms from Eqs. (50)-(55), the two additional constraint equations are derived as follows:

$$\bar{S}_{1i,j,k}^{xyt} = \bar{S}_{2i,j,k}^{xyt} + \bar{S}_{3i,j,k}^{xyt} + \bar{f}_{xi,j,k}^{xyt} \quad (68)$$

$$\bar{S}_{4i,j,k}^{xyt} = \bar{S}_{5i,j,k}^{xyt} + \bar{S}_{6i,j,k}^{xyt} + \bar{f}_{yi,j,k}^{xyt} \quad (69)$$

To eliminate the surface-averaged terms in Eq. (62)-(69), we derive expressions for each surface-averaged variable in terms of cell-centered values. This requires solving the six ODEs in Eq. (50)-(55) analytically. The solution procedure for these ODEs follows the methodology outlined in Section 2.1.2. Specifically, the space-averaged ODEs (Eq. (52) and Eq. (55)) are solved using an approach analogous to that for Eq. (10) in the one-dimensional case, yielding expressions for $\bar{u}_{i,j,k}^{xy}$ and $\bar{v}_{i,j,k}^{xy}$. Similarly, the remaining four space-time averaged ODEs (Eqs. (50), (51), (53), and (54)) are solved using a process similar to the solution of Eq. (11) in the one-dimensional case. However, it is important to note a key distinction in boundary conditions between the one-dimensional and two-dimensional scenarios for the solution of these remaining four ODEs. In the one-dimensional case, line-averaged velocities ($\bar{u}_{i,j}^t$) and flux ($\bar{J}_{i,j}^t$) serve as local boundary conditions. In contrast, the two-dimensional case requires plane-averaged velocities ($\bar{u}_{i,j,k}^{xt}$, $\bar{u}_{i,j,k}^{yt}$, $\bar{v}_{i,j,k}^{xt}$ and $\bar{v}_{i,j,k}^{yt}$) and fluxes ($\bar{J}_{xi,j,k}^{xt}$, $\bar{J}_{xi,j,k}^{yt}$, $\bar{J}_{yi,j,k}^{xt}$ and $\bar{J}_{yi,j,k}^{yt}$) as local boundary conditions for solving these ODEs analytically. Subsequently, the continuity condition, as discussed in Section 0, is applied in a manner analogous to the one-dimensional case to ensure consistency at the shared edges of adjacent nodes. This process allows for the derivation of expressions for surface-averaged velocities ($\bar{u}_{i,j,k}^{xy}$, $\bar{u}_{i,j,k}^{xt}$, $\bar{u}_{i,j,k}^{yt}$, $\bar{v}_{i,j,k}^{xy}$, $\bar{v}_{i,j,k}^{xt}$ and $\bar{v}_{i,j,k}^{yt}$) and fluxes ($\bar{J}_{xi,j,k}^{xt}$, $\bar{J}_{xi,j,k}^{yt}$, $\bar{J}_{yi,j,k}^{xt}$ and $\bar{J}_{yi,j,k}^{yt}$) in the two-dimensional framework, as detailed below:

$$\bar{u}_{i,j,k}^{xy} = \bar{u}_{i,j,k}^{xyt} + \tau_j \bar{S}_{1i,j,k}^{xyt} \quad (70)$$

$$\bar{u}_{i,j,k}^{yt} = \frac{A_{32} \bar{S}_{3i,j,k}^{xyt} - A_{52,i+1} \bar{S}_{3i+1,j,k}^{xyt} + A_{31} \bar{u}_{i,j,k}^{xyt} - A_{51,i+1} \bar{u}_{i+1,j,k}^{xyt}}{A_{31} - A_{51,i+1}} \quad (71)$$

$$\bar{u}_{i,j,k}^{xt} = \frac{B_{32} \bar{S}_{2i,j,k}^{xyt} - B_{52,j+1} \bar{S}_{2i,j+1,k}^{xyt} + B_{31} \bar{u}_{i,j,k}^{xyt} - B_{51,j+1} \bar{u}_{i,j+1,k}^{xyt}}{B_{31} - B_{51,j+1}} \quad (72)$$

$$\bar{J}_{xi,j,k}^{yt} = \frac{-A_{32} A_{51,i+1} \bar{S}_{3i,j,k}^{xyt} + A_{31} A_{52,i+1} \bar{S}_{3i+1,j,k}^{xyt} + A_{31} A_{51,i+1} (\bar{u}_{i+1,j,k}^{xyt} - \bar{u}_{i,j,k}^{xyt})}{A_{31} - A_{51,i+1}} \quad (73)$$

$$\bar{J}_{xi,j,k}^{xt} = \frac{-B_{32} B_{51,j+1} \bar{S}_{2i,j,k}^{xyt} + B_{31} B_{52,j+1} \bar{S}_{2i,j+1,k}^{xyt} + B_{31} B_{51,j+1} (\bar{u}_{i,j+1,k}^{xyt} - \bar{u}_{i,j,k}^{xyt})}{B_{31} - B_{51,j+1}} \quad (74)$$

$$\bar{v}_{i,j,k}^{xy} = \bar{v}_{i,j,k}^{xyt} + \tau_j \bar{S}_{4i,j,k}^{xyt} \quad (75)$$

$$\bar{v}_{i,j,k}^{yt} = \frac{A_{32} \bar{S}_{6i,j,k}^{xyt} - A_{52,i+1} \bar{S}_{6i+1,j,k}^{xyt} + A_{31} \bar{v}_{i,j,k}^{xyt} - A_{51,i+1} \bar{v}_{i+1,j,k}^{xyt}}{A_{31} - A_{51,i+1}} \quad (76)$$

$$\bar{v}_{i,j,k}^{xt} = \frac{B_{32} \bar{S}_{5i,j,k}^{xyt} - B_{52,j+1} \bar{S}_{5i,j+1,k}^{xyt} + B_{31} \bar{v}_{i,j,k}^{xyt} - B_{51,j+1} \bar{v}_{i,j+1,k}^{xyt}}{B_{31} - B_{51,j+1}} \quad (77)$$

$$\bar{J}_{yi,j,k}^{yt} = \frac{-A_{32} A_{51,i+1} \bar{S}_{6i,j,k}^{xyt} + A_{31} A_{52,i+1} \bar{S}_{6i+1,j,k}^{xyt} + A_{31} A_{51,i+1} (\bar{v}_{i+1,j,k}^{xyt} - \bar{v}_{i,j,k}^{xyt})}{A_{31} - A_{51,i+1}} \quad (78)$$

$$\bar{J}_{yi,j,k}^{xt} = \frac{-B_{32} B_{51,j+1} \bar{S}_{5i,j,k}^{xyt} + B_{31} B_{52,j+1} \bar{S}_{5i,j+1,k}^{xyt} + B_{31} B_{51,j+1} (\bar{v}_{i,j+1,k}^{xyt} - \bar{v}_{i,j,k}^{xyt})}{B_{31} - B_{51,j+1}} \quad (79)$$

By modifying the indexing in the relevant equations as follows—changing (i, j, k) to $(i, j, k - 1)$ in Eqs. (70) and (75), (i, j, k) to $(i - 1, j, k)$ in Eqs. (71), (73), (76), and (78), and (i, j, k) to $(i, j - 1, k)$ in Eqs. (72), (74), (77), and (79)—we can derive expressions for $\bar{u}_{i,j,k-1}^{xy}$, $\bar{v}_{i,j,k-1}^{xy}$, $\bar{u}_{i-1,j,k}^{yt}$, $\bar{u}_{i,j-1,k}^{xt}$, $\bar{v}_{i-1,j,k}^{yt}$, $\bar{v}_{i,j-1,k}^{xt}$, $\bar{J}_{xi-1,j,k}^{yt}$, $\bar{J}_{xi,j-1,k}^{xt}$, $\bar{J}_{yi-1,j,k}^{yt}$, $\bar{J}_{yi,j-1,k}^{xt}$. By substituting all these surface-averaged expressions derived from Eqs. (70)-(79) into the constraint equations (Eqs. (62)-(69)), we obtain eight algebraic equations per node in terms of cell-centered variables, as stated below:

$$\bar{S}_{3i,j,k}^{xyt} = \frac{\bar{S}_{1i,j,k}^{xyt} - \bar{S}_{1i,j,k-1}^{xyt}}{2} + \frac{\bar{u}_{i,j,k}^{xyt} - \bar{u}_{i,j,k-1}^{xyt}}{2\tau_k} + F_{51} \bar{S}_{2i,j,k}^{xyt} + F_{52} \bar{S}_{2i,j-1,k}^{xyt} + F_{53} \bar{S}_{2i,j+1,k}^{xyt} + F_{54} \bar{u}_{i,j,k}^{xyt} + F_{55} \bar{u}_{i,j-1,k}^{xyt} + F_{56} \bar{u}_{i,j+1,k}^{xyt} - \bar{f}_{xi,j,k}^{xyt} \quad (80)$$

$$\bar{S}_{2i,j,k}^{xyt} = \frac{\bar{S}_{1i,j,k}^{xyt} - \bar{S}_{1i,j,k-1}^{xyt}}{2} + \frac{\bar{u}_{i,j,k}^{xyt} - \bar{u}_{i,j,k-1}^{xyt}}{2\tau_k} + F_{31} \bar{S}_{3i,j,k}^{xyt} + F_{32} \bar{S}_{3i-1,j,k}^{xyt} + F_{33} \bar{S}_{3i+1,j,k}^{xyt} + F_{34} \bar{u}_{i,j,k}^{xyt} + F_{35} \bar{u}_{i-1,j,k}^{xyt} + F_{36} \bar{u}_{i+1,j,k}^{xyt} - \bar{f}_{xi,j,k}^{xyt} \quad (81)$$

$$\begin{aligned} \bar{S}_{1i,j,k}^{xyt} = & -(F_{31}\bar{S}_{3i,j,k}^{xyt} + F_{32}\bar{S}_{3i-1,j,k}^{xyt} + F_{33}\bar{S}_{3i+1,j,k}^{xyt} + F_{34}\bar{u}_{i,j,k}^{xyt} + F_{35}\bar{u}_{i-1,j,k}^{xyt} + \\ & F_{36}\bar{u}_{i+1,j,k}^{xyt}) - (F_{51}\bar{S}_{2i,j,k}^{xyt} + F_{52}\bar{S}_{2i,j-1,k}^{xyt} + F_{53}\bar{S}_{2i,j+1,k}^{xyt} + F_{54}\bar{u}_{i,j,k}^{xyt} + F_{55}\bar{u}_{i,j-1,k}^{xyt} + \\ & F_{56}\bar{u}_{i,j+1,k}^{xyt}) + \bar{f}_{xi,j,k}^{xyt} \end{aligned} \quad (82)$$

$$\begin{aligned} \bar{u}_{i,j,k}^{xyt} = & M_{51}\bar{S}_{3i,j,k}^{xyt} + M_{52}\bar{S}_{3i-1,j,k}^{xyt} + M_{53}\bar{S}_{3i+1,j,k}^{xyt} + M_{54}\bar{u}_{i-1,j,k}^{xyt} + M_{55}\bar{u}_{i+1,j,k}^{xyt} + \\ & N_{51}\bar{S}_{2i,j,k}^{xyt} + N_{52}\bar{S}_{2i,j-1,k}^{xyt} + N_{53}\bar{S}_{2i,j+1,k}^{xyt} + N_{54}\bar{u}_{i,j-1,k}^{xyt} + N_{55}\bar{u}_{i,j+1,k}^{xyt} + L_{51}\bar{S}_{1i,j,k}^{xyt} - \\ & L_{52}\bar{S}_{1i,j,k-1}^{xyt} + L_{53}\bar{u}_{i,j,k-1}^{xyt} + L_{54}\bar{f}_{xi,j,k}^{xyt} \end{aligned} \quad (83)$$

$$\begin{aligned} \bar{S}_{6i,j,k}^{xyt} = & \frac{\bar{S}_{4i,j,k}^{xyt} - \bar{S}_{4i,j,k-1}^{xyt}}{2} + \frac{\bar{v}_{i,j,k}^{xyt} - \bar{v}_{i,j,k-1}^{xyt}}{2\tau_k} + F_{51}\bar{S}_{5i,j,k}^{xyt} + F_{52}\bar{S}_{5i,j-1,k}^{xyt} + F_{53}\bar{S}_{5i,j+1,k}^{xyt} + \\ & F_{54}\bar{v}_{i,j,k}^{xyt} + F_{55}\bar{v}_{i,j-1,k}^{xyt} + F_{56}\bar{v}_{i,j+1,k}^{xyt} - \bar{f}_{yi,j,k}^{xyt} \end{aligned} \quad (84)$$

$$\begin{aligned} \bar{S}_{5i,j,k}^{xyt} = & \frac{\bar{S}_{4i,j,k}^{xyt} - \bar{S}_{4i,j,k-1}^{xyt}}{2} + \frac{\bar{v}_{i,j,k}^{xyt} - \bar{v}_{i,j,k-1}^{xyt}}{2\tau_k} + F_{31}\bar{S}_{6i,j,k}^{xyt} + F_{32}\bar{S}_{6i-1,j,k}^{xyt} + F_{33}\bar{S}_{6i+1,j,k}^{xyt} + \\ & F_{34}\bar{v}_{i,j,k}^{xyt} + F_{35}\bar{v}_{i-1,j,k}^{xyt} + F_{36}\bar{v}_{i+1,j,k}^{xyt} - \bar{f}_{yi,j,k}^{xyt} \end{aligned} \quad (85)$$

$$\begin{aligned} \bar{S}_{4i,j,k}^{xyt} = & -(F_{31}\bar{S}_{6i,j,k}^{xyt} + F_{32}\bar{S}_{6i-1,j,k}^{xyt} + F_{33}\bar{S}_{6i+1,j,k}^{xyt} + F_{34}\bar{v}_{i,j,k}^{xyt} + F_{35}\bar{v}_{i-1,j,k}^{xyt} + \\ & F_{36}\bar{v}_{i+1,j,k}^{xyt}) - (F_{51}\bar{S}_{5i,j,k}^{xyt} + F_{52}\bar{S}_{5i,j-1,k}^{xyt} + F_{53}\bar{S}_{5i,j+1,k}^{xyt} + F_{54}\bar{v}_{i,j,k}^{xyt} + F_{55}\bar{v}_{i,j-1,k}^{xyt} + \\ & F_{56}\bar{v}_{i,j+1,k}^{xyt}) + \bar{f}_{yi,j,k}^{xyt} \end{aligned} \quad (86)$$

$$\begin{aligned} \bar{v}_{i,j,k}^{xyt} = & M_{51}\bar{S}_{6i,j,k}^{xyt} + M_{52}\bar{S}_{6i-1,j,k}^{xyt} + M_{53}\bar{S}_{6i+1,j,k}^{xyt} + M_{54}\bar{v}_{i-1,j,k}^{xyt} + M_{55}\bar{v}_{i+1,j,k}^{xyt} + \\ & N_{51}\bar{S}_{5i,j,k}^{xyt} + N_{52}\bar{S}_{5i,j-1,k}^{xyt} + N_{53}\bar{S}_{5i,j+1,k}^{xyt} + N_{54}\bar{v}_{i,j-1,k}^{xyt} + N_{55}\bar{v}_{i,j+1,k}^{xyt} + L_{51}\bar{S}_{4i,j,k}^{xyt} - \\ & L_{52}\bar{S}_{4i,j,k-1}^{xyt} + L_{53}\bar{v}_{i,j,k-1}^{xyt} + L_{54}\bar{f}_{yi,j,k}^{xyt} \end{aligned} \quad (87)$$

It is important to note that every coefficient in the final set of algebraic equations (Eqs. (80)-(87)) is dependent upon the velocities at the current time step (i.e., $\bar{u}_{i,j,k}^0$ and $\bar{v}_{i,j,k}^0$), introducing nonlinearity to the entire system. Detailed definitions for all the A 's, B 's and F 's, G 's, L 's, M 's, N 's coefficients for two-dimensional case are listed in Appendix A.

2.2.1 Derivation of nonlinear convective velocities

The definition of the convective velocities in MNIM for the two-dimensional case is given as

$$\bar{u}_{i,j,k}^0 = \frac{\bar{u}_{i,j,k}^{yt} + \bar{u}_{i-1,j,k}^{yt} + \bar{u}_{i,j,k}^{xt} + \bar{u}_{i,j-1,k}^{xt}}{4} \quad (88)$$

$$\bar{v}_{i,j,k}^0 = \frac{\bar{v}_{i,j,k}^{yt} + \bar{v}_{i-1,j,k}^{yt} + \bar{v}_{i,j,k}^{xt} + \bar{v}_{i,j-1,k}^{xt}}{4} \quad (89)$$

Similar to the one-dimensional case, by using Eqs. (70)-(79), which establish the relationship between the surface-averaged and cell-centered values, and substituting the expressions from these equations into Eq. (88), we obtain:

$$\begin{aligned} \bar{u}_{i,j,k}^0 = & F_{71}\bar{S}_{3i-1,j,k}^{ytx} + F_{72}\bar{S}_{3i,j,k}^{ytx} + F_{73}\bar{S}_{3i+1,j,k}^{ytx} + F_{74}\bar{u}_{i-1,j,k}^{xyt} + F_{75}\bar{u}_{i,j,k}^{xyt} + \\ & F_{76}\bar{u}_{i+1,j,k}^{xyt} + G_{71}\bar{S}_{2i,j-1,k}^{xty} + G_{72}\bar{S}_{2i,j,k}^{xty} + G_{73}\bar{S}_{2i,j+1,k}^{xty} + G_{74}\bar{u}_{i,j-1,k}^{xyt} + G_{75}\bar{u}_{i,j,k}^{xyt} + \\ & G_{76}\bar{u}_{i,j+1,k}^{xyt} \end{aligned} \quad (90)$$

All the F 's and G 's coefficients are listed in Appendix A. The other equation for $\bar{v}_{i,j,k}^0$ can be obtained in a similar manner.

3 Numerical tests

In this section, we present results from applying the developed MCCNIM scheme to three Burgers' problems, comprising two one-dimensional cases and one two-dimensional cases, each with a known analytical solution. For the first example, we include error tables and plots to examine the spatial and temporal convergence of the scheme. In the second example, we provide a detailed comparison of our results and errors with the classical NIM approach and other schemes, showcasing the effectiveness of the developed MCCNIM approach. For the two-dimensional cases, we solve a problem to validate the performance of the scheme. It is noteworthy that in both one- and two-dimensional cases, the algebraic equations from the discretization are iteratively solved using the Picard-based method at each time step.

We compute RMS error (in one-dimension) using,

$$RMS = \sqrt{\frac{\sum_{i=1}^{n_x} |\bar{u}_{i,k}^{xt} - u_{i,k}^{exact}|^2}{n_x}} \quad (91)$$

Where n_x are the spatial grid-points and k is the time-index in one-dimensional problems. It is clear from Eq. (91) that the RMS error is calculated at the final time step, consistently applied across both one-dimensional and two-dimensional problems throughout the paper.

A distinctive feature of the MCCNIM is its averaging of discrete variables over nodes, in contrast to finite-difference methods, which perform computations at grid points. As a result, precise quantitative error analysis in MCCNIM requires the node-averaged exact solution.

Although calculating the node-averaged exact solution analytically is straightforward in some cases, it presents challenges in most others. Therefore, we employ numerical integration using built-in functions of MATLAB to determine the node-averaged values, ensuring an accurate comparison for our numerical scheme. In each test case, we average the exact solution by performing numerical integration in MATLAB over the node's width $2a$ (from $x_c - a$ to $x_c + a$) and height 2τ (from $(t_f - 2\tau)$ to t_f), then divided by $4a\tau$. Here, x_c represents centroid of the corresponding node and t_f is the current time step.

In this study, we employed the most recent version of MATLAB (R2023a) as our integrated development environment and compiler for code generation and execution. Our simulations are conducted on a system powered by an Intel(R) Core (TM) i7-7700 CPU @ 3.60 GHz, featuring four Cores, eight Logical processors and a substantial 16 GB of RAM.

Example 1 The first test problem is concerned with the one-dimensional Burgers' equation which involves an initial sinusoidal wave that propagates and diffuses within a confined flow domain along the x-direction. The problem is subject to the initial condition

$$u(x, 0) = \sin(\pi x), \quad 0 < x < 1 \quad (92)$$

and following homogenous Dirichlet boundary conditions

$$u(0, t) = u(1, t) = 0, \quad 0 \leq t \leq T \quad (93)$$

The exact Fourier solution to this problem, represented by an infinite series, is given as:

$$u(x, t) = \frac{2\pi \sum_{k=1}^{\infty} C_k e^{-\left(\frac{k^2 \pi^2 t}{Re}\right) k \sin(k\pi x)}}{C_0 + \sum_{k=1}^{\infty} C_k e^{-\left(\frac{k^2 \pi^2 t}{Re}\right) \cos(k\pi x)}}, \quad (94)$$

where the Fourier coefficients are given as

$$C_0 = \int_0^1 e^{-\frac{Re}{2\pi}(1-\cos(\pi x))} dx$$

$$C_k = 2 \int_0^1 e^{-\frac{Re}{2\pi}(1-\cos(\pi x))} \cos(k\pi x) dx, \quad k = 1, 2, 3, \dots$$

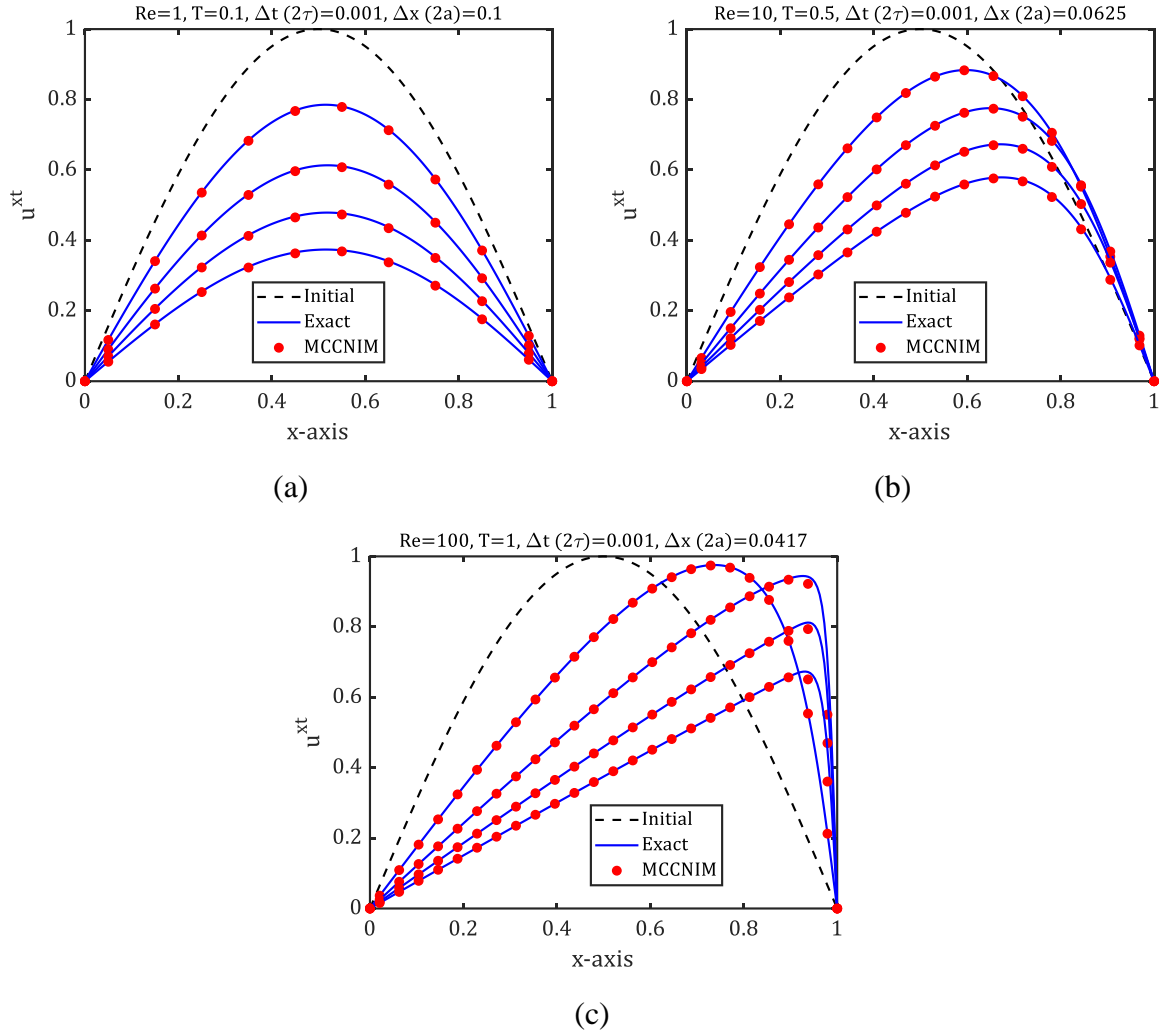


Figure 5: Comparison of the numerical solution obtained using the MCCNIM scheme for **Example 1** with the exact solution at interval of $T/4$ for three different values of Reynolds numbers: (a) $Re = 1$, (b) $Re = 10$, (c) $Re = 100$.

To validate the proposed scheme, the numerical results are compared with the exact solution for three different Reynolds number: $Re = 1$, $Re = 10$, and $Re = 100$, as illustrated in Figure 5. The simulations are conducted up to the total time of $T = 0.1$ sec for $Re = 1$, $T = 0.5$ sec for $Re = 10$, and $T = 1$ sec for $Re = 100$. In each case, the numerical and exact solution are compared at interval of $T/4$. The numerical solution aligns closely with the exact solution in all cases. For instance, in the case of $Re = 1$, as shown in panel (a) of Figure 5, only $n_x = 10$ grid points are sufficient to achieve an accurate match with the exact solution. This demonstrates that the developed scheme effectively maintains the accuracy characteristic of coarse-mesh methods.

Table 1 RMS errors for different node sizes in **Example 1**. The numerical solution is calculated at the final time step with $T = 0.1$ for $Re = 1$, $T = 0.2$ for $Re = 10$, and $T = 0.3$ for $Re = 50$.

Node size $\Delta x (2a)$	RMS errors		
	$Re = 1$	$Re = 10$	$Re = 50$
0.5	1.70E-02	7.22E-02	9.77E-02
0.25	5.42E-03	1.73E-02	9.63E-02
0.125	1.51E-03	4.65E-03	4.11E-02
0.0625	3.96E-04	1.23E-03	9.86E-03
0.03125	9.81E-05	3.16E-04	2.54E-03
0.015625	4.63E-06	7.89E-05	6.51E-04

For each simulation, the tolerance is set to 1×10^{-06} with a smaller timestep size $\Delta t = 0.001$.

Table 2 RMS errors for different timestep sizes in **Example 1**.

Timestep size $\Delta t (2\tau)$	RMS errors at $T = 0.1$ second		
	$Re = 1$	$Re = 10$	$Re = 50$
0.1	4.18E-02	6.66E-03	5.80E-03
0.05	5.91E-03	1.42E-03	1.50E-03
0.025	1.00E-03	3.33E-04	3.80E-04
0.0125	2.16E-04	8.23E-05	9.72E-05
0.0050	3.66E-05	1.92E-05	2.27E-05

For each simulation, the tolerance is set to 1×10^{-06} with a fine node size $\Delta x = 0.0125$

Moreover, we computed the RMS errors using different grid sizes for a range of Reynolds values in order to further illustrate the efficacy of our established method. We used a smaller time step ($\Delta t=0.001$) and calculated RMS errors for a range of Reynolds values while altering the grid sizes to illustrate the convergence order of our technique, as shown in Table 1. The RMS errors are shown against node sizes in panel (a) of Figure 6 to visually represent the outcomes of these error computations. Interestingly, the figure shows a slope of around 2 in each case, indicating that our numerical approach has second-order accuracy in space. Similarly, Table 2 lists the RMS errors at the fine node size ($\Delta x=0.001$) for different time step sizes, which are presented in panel (b) of Figure 6 to analyse the order in time. The lines in

panel (b) of Figure 6 has the slopes that are very near to 2, indicating second-order temporal accuracy. This crucial demonstration emphasizes that even when working with higher Reynolds numbers and varying time step sizes, our computational method retains its second-order precision.

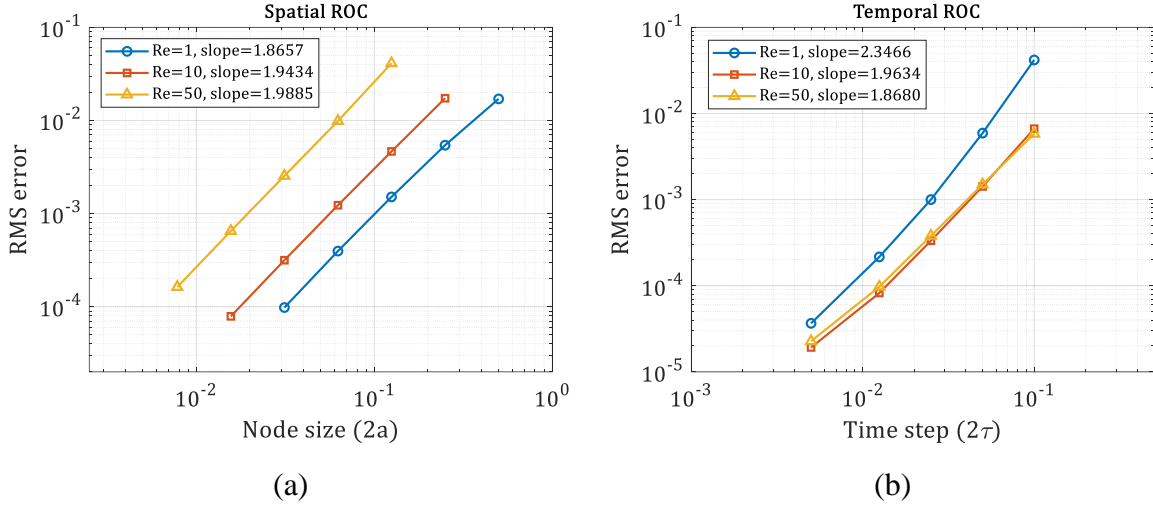
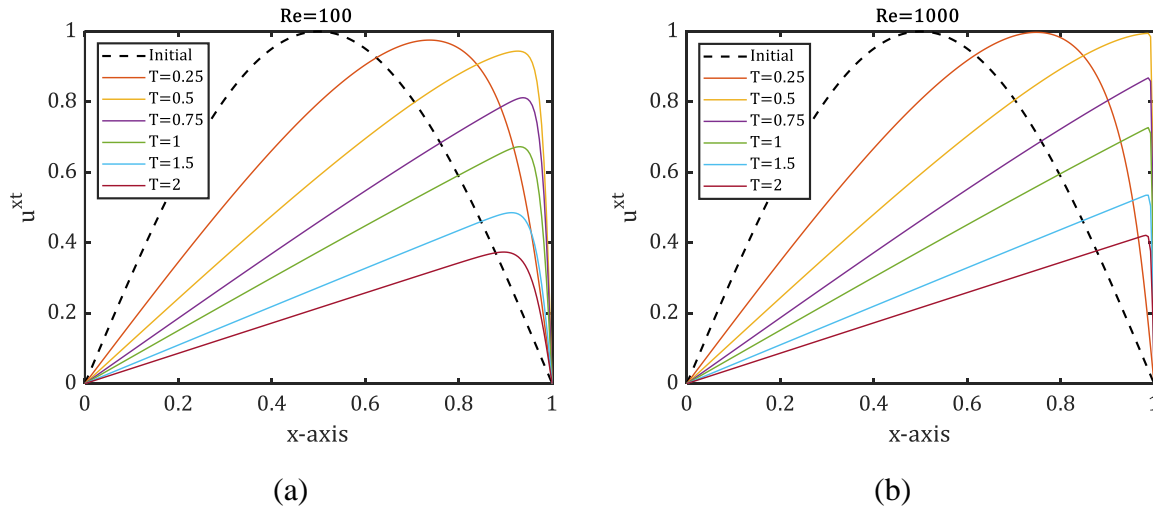
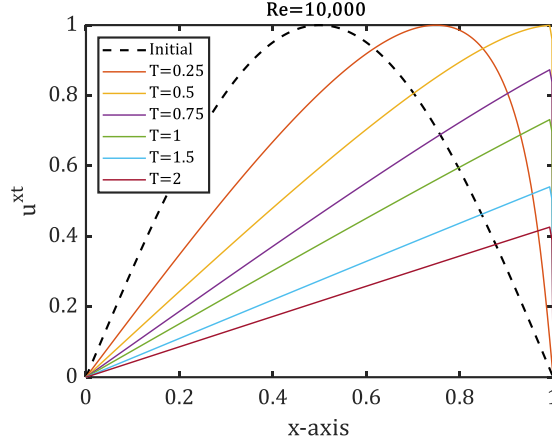


Figure 6 Rate of convergence (ROC) for **Example 1** at three different values of Re . (a) Spatial rate of convergence. (b) Temporal rate of convergence.

In Figure 5, we present both numerical (red solid dots) and exact (blue solid lines) solution curves for various Reynolds numbers ($Re = 1, 10, \text{ and } 100$), demonstrating good agreement in each case. However, for higher Reynolds numbers, such as $Re = 1000$, the infinite series fails to converge. Therefore, to validate the scheme for problems with high nonlinearity (i.e., high Reynolds numbers), we computed numerical results for larger Reynolds numbers at different time points, as shown in Figure 7. Figure 7 confirms that the scheme performs effectively at higher Reynolds numbers, as the curves exhibit the expected physical behaviour.





(c)

Figure 7 Numerical solutions for **Example 1** at higher Reynolds numbers using $\Delta x = 0.0125$ and $\Delta t = 0.01$: (a) $Re = 100$, (b) $Re = 1000$, (c) $Re = 10,000$.

Example 2: One-Dimensional Propagating Shock Problem [14]

The governing equation for the propagating Shock problem is given by

$$\frac{\partial u(x,t)}{\partial t} + u(x,t) \frac{\partial u(x,t)}{\partial x} = \frac{1}{Re} \frac{\partial^2 u(x,t)}{\partial x^2} \quad x \in [-2,2] \quad (95)$$

The initial and boundary conditions are

$$u(x, 0) = \frac{1}{2} \left[1 - \tanh \left(\frac{xRe}{4} \right) \right], \quad (96)$$

$$u(-2, t) = \frac{1}{2} \left[1 - \tanh \left(-\frac{Re}{2} - \frac{tRe}{8} \right) \right], \quad (97)$$

$$u(+2, t) = \frac{1}{2} \left[1 - \tanh \left(\frac{Re}{2} - \frac{tRe}{8} \right) \right]. \quad (98)$$

The exact solution is

$$u(x, t) = \frac{1}{2} \left[1 - \tanh \left(\frac{xRe}{4} - \frac{tRe}{8} \right) \right]. \quad (99)$$

Using the scenario described in reference [22], we compare the precise solution with the solution derived using the MCCNIM scheme in panel (a) of Figure 8. We expand our study to very high Reynolds numbers ($Re=10^6$) in order to better illustrate the scheme's resilience. When using a large timestep size (i.e., $\Delta t=0.1$) and coarser grid size (i.e., $\Delta x=0.1$), the

technique described here follow the propagation front very well, even in the situation of very high Reynolds numbers, as shown in panel (a) of Figure 8.

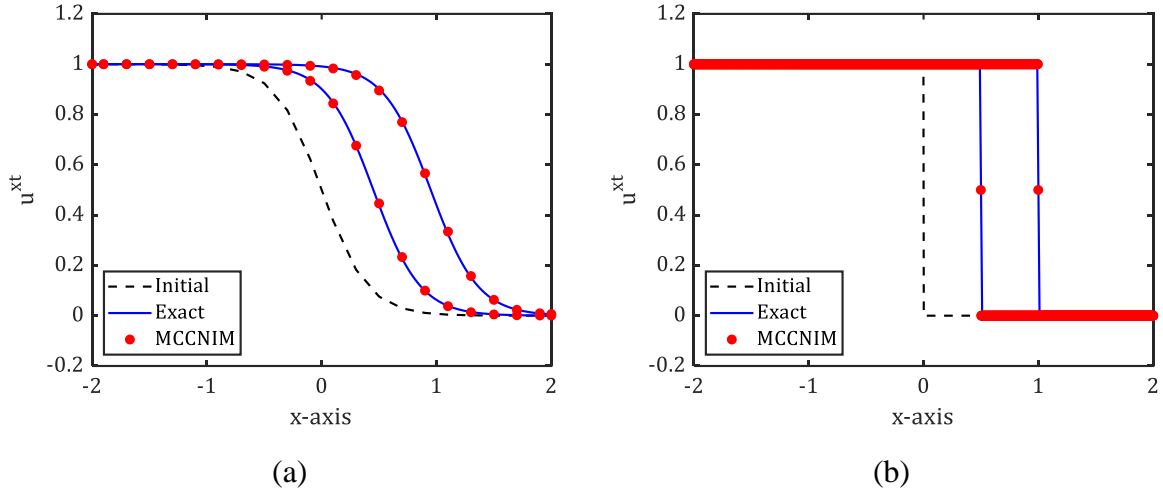
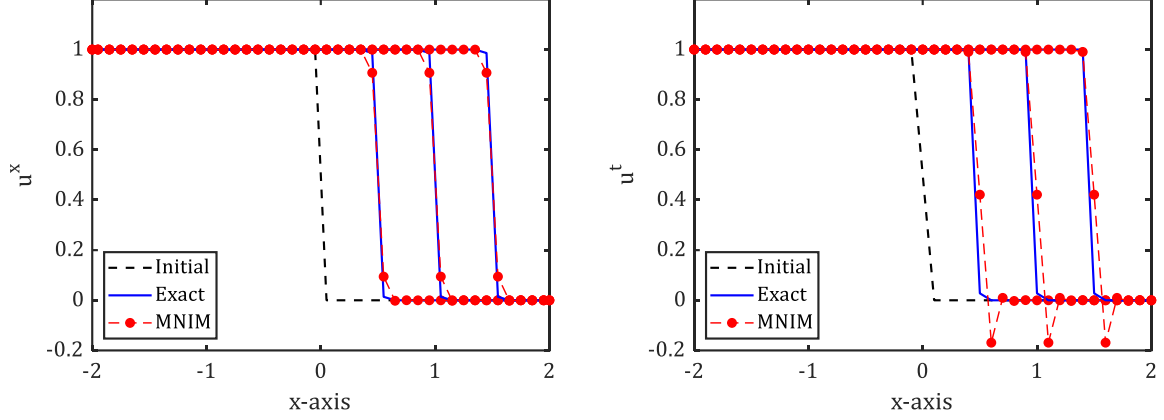


Figure 8 Comparison of numerical and exact solution for **Example 2** at $t=1$ and $t=2$ seconds. (a) $Re=10$, $\Delta x=0.2$, and $\Delta t=0.2$. (b) $Re=10^6$, $\Delta x=0.003125$, and $\Delta t=0.00625$.

The chosen test problem has also been used in the literature to compare the modified NIM (or MNIM) with another scheme called the Crank-Nicolson 4-Point Upwind (CN-4PU) scheme. When comparing the RMS errors of the two schemes, it was shown that the MNIM performs noticeably better than CN-4PU. Therefore, in Table 3, using the identical error comparison cases, we are also confirming that our scheme is either better than or equal to the MNIM [14].

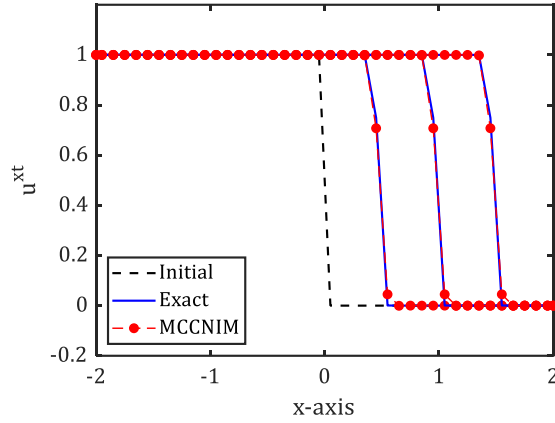
In the first case described for MNIM [14], where $Re=300$ at $t=1.5$ seconds with 100 nodes and $\Delta t=0.05$, the RMS errors for space-averaged surface (\bar{u}^x), time-averaged surface (\bar{u}^t), and both \bar{u}^x and \bar{u}^t values are 0.1562×10^{-2} , 0.1002×10^{-1} and 0.7155×10^{-2} , respectively. In contrast, the RMS error in MCCNIM for the identical case is 0.4148×10^{-2} , which shows a decrease. It is critical to understand that the analytical solution used to calculate RMS error differs between MCCNIM and MNIM. The analytical solution is averaged over the surface, either spatially or temporally, in MNIM, as described in the work of Rizwan-Uddin [14]. On the other hand, the analytical solution is averaged across the whole cell in MCCNIM, including both temporal and spatial dimensions. As a result, precise accuracy may not be obtained when comparing the cell-centered value in MCCNIM with the surface-averaged value in MNIM. It still offers a reasonable comparison, though. For example, the error discrepancy between \bar{u}^x (space-averaged surface), \bar{u}^t (time-averaged surface), and the average of both \bar{u}^x and \bar{u}^t values are substantially smaller in the case of $Re=300$. It would be preferable to use the averaged error

of both surface-averaged values (i.e., the average of both \bar{u}^x and \bar{u}^t) when comparing MCCNIM with NIM [22].



(a) \bar{u}^x vs exact \bar{u}^x (MNIM)

(b) \bar{u}^t vs exact \bar{u}^t (MNIM)



(c) \bar{u}^{xt} vs exact \bar{u}^{xt} (developed MCCNIM)

Figure 9 Numerical vs. Analytical Solutions: MNIM and MCCNIM comparison at $t=1$, $t=2$, and $t=3$ for **Example 2**, $Re=1000$, nodes=40, $dt=0.1$. RMS errors for MNIM: with \bar{u}^x values

are 1.781×10^{-3} , with \bar{u}^t values are 6.862×10^{-2} , and with \bar{u}^x and \bar{u}^t values are

4.985×10^{-2} . RMS errors in MCCNIM with \bar{u}^{xt} values are 9.415×10^{-3}

In Figure 9, we present a comparison between the exact solution and the results obtained from both the MNIM and MCCNIM schemes under the conditions of $Re=1000$ and $dt=0.1$, observed at three distinct time points ($t=1$, $t=2$, and $t=3$). Due to distinct errors associated with these variables, we present two separate figures for MNIM: Panel (a) of Figure 9 illustrates the comparison of the solution of \bar{u}^x with the exact \bar{u}^x , while Panel (b) depicts the solution of \bar{u}^t in comparison with the exact \bar{u}^t . In Panel (c), the solution of the developed scheme (MCCNIM) for \bar{u}^{xt} is contrasted with the exact \bar{u}^{xt} solution.

Table 3 Comparison of RMS errors of MCCNIM vs. CN-4PU, CNIM, and MNIM [14].
($\Delta t=0.1$; 20 nodes)

		$Re = 50$		$Re = 100$	
		$t = 1.0$	$t = 3.0$	$t = 1.0$	$t = 3.0$
CN-4PU		3.652×10^{-2}	3.524×10^{-2}	4.546×10^{-2}	4.367×10^{-2}
CNIM		3.091×10^{-2}	3.068×10^{-2}	6.558×10^{-2}	6.376×10^{-2}
	\bar{u}^x	1.338×10^{-2}	1.382×10^{-2}	1.172×10^{-2}	1.185×10^{-2}
MNIM	\bar{u}^t	2.721×10^{-2}	2.775×10^{-2}	2.666×10^{-2}	2.678×10^{-2}
	\bar{u}^x and \bar{u}^t	2.127×10^{-2}	2.175×10^{-2}	2.041×10^{-2}	2.053×10^{-2}
MCCNIM	\bar{u}^{xt}	1.649×10^{-2}	1.722×10^{-2}	1.648×10^{-2}	1.688×10^{-2}

As depicted in Panel (c) of Figure 9, the MCCNIM demonstrates highly accurate tracking of the wave front even at high Reynolds numbers, with an RMS error of 9.415×10^{-3} . This precision is achieved with minimal oscillation and without the necessity for artificial dissipation. In contrast, for MNIM, the comparison of \bar{u}^x with the exact \bar{u}^x is notably accurate, featuring a low RMS error of 1.781×10^{-3} . However, when assessing \bar{u}^t against the exact \bar{u}^t , a higher RMS error is observed, measuring 6.862×10^{-2} , as illustrated in Panel (b) of Figure 9. Given that the total error incorporates both \bar{u}^x and \bar{u}^t errors, the combined RMS error is 4.985×10^{-2} , exceeding the overall error in MNIM. Additional information regarding the quantitative comparison of RMS errors between MCCNIM and MNIM, along with errors from various other schemes as provided by Rizwan-Uddin [14], is presented in Error! Reference source not found..

A comprehensive analysis of RMS errors has been presented in Table 4 and Table 5, drawing comparisons between MCCNIM, MNIM, and M^2 NIM across a spectrum of scenarios involving varying Reynolds numbers, node sizes, and time steps. The results unequivocally demonstrate that, even in the case of the nonlinear Burgers' equation, MCCNIM consistently outperforms other traditional NIMs developed thus far for fluid flow applications.

Table 4 Comparison of RMS errors of developed MCCNIM with MNIM and M²NIM [24].
(Re=100 and $t=2.0$ sec)

		RMS errors ($\times 10^{-2}$)		
		MNIM	M ² NIM	MCCNIM
$\Delta x = 0.2$	$\Delta t = 0.02$	4.88	4.75	2.61
	$\Delta t = 0.01$	4.61	4.56	2.67
	$\Delta t = 0.005$	4.48	4.45	2.69
$\Delta x = 0.1$	$\Delta t = 0.02$	2.15	1.94	1.44
	$\Delta t = 0.01$	2.02	1.95	1.49
	$\Delta t = 0.005$	1.95	1.92	1.52
$\Delta x = 0.05$	$\Delta t = 0.02$	0.759	0.601	0.615
	$\Delta t = 0.01$	0.757	0.679	0.644
	$\Delta t = 0.005$	0.752	0.730	0.653

Table 5 Comparison of RMS errors of developed MCCNIM with MNIM and M²NIM [24].
(Re=200 and $t=2.0$ sec)

		RMS errors ($\times 10^{-2}$)		
		MNIM	M ² NIM	MCCNIM
$\Delta x = 0.2$	$\Delta t = 0.02$	6.36	6.59	3.01
	$\Delta t = 0.01$	6.20	6.12	3.08
	$\Delta t = 0.005$	5.90	5.87	3.11
$\Delta x = 0.1$	$\Delta t = 0.02$	3.77	3.45	1.79
	$\Delta t = 0.01$	3.43	3.33	1.89
	$\Delta t = 0.005$	3.24	3.20	1.93
$\Delta x = 0.05$	$\Delta t = 0.02$	1.66	1.29	0.92
	$\Delta t = 0.01$	1.51	1.33	1.03
	$\Delta t = 0.005$	1.42	1.37	1.07

It is important to highlight that the error values utilized for comparison in this work have been sourced from the existing literature. We have conducted a thorough analysis of the MNIM code created in this work to make sure it is accurate and consistent with previous research, which has enabled us to determine similar parameters, such as tolerance levels, enabling an honest

and equitable comparison of MCCNIM with other schemes. Furthermore, obtaining the RMS errors for MCCNIM requires node-averaged values (i.e., \bar{u}^{xt}), and due to the impracticality of analytically integrating the exact solution provided by Eq. (99) in both spatial and temporal directions, MATLAB software was employed for averaging. The same averaging technique was rigorously tested for comparing surface-averaged errors in MNIM, and the results precisely corresponded with those reported in the reference papers [14,24]. This meticulous approach ensures the validity and reliability of the comparative analysis, which increases trust in the correctness of the results.

Example 3: Two-Dimensional Propagating Shock Problem [24]

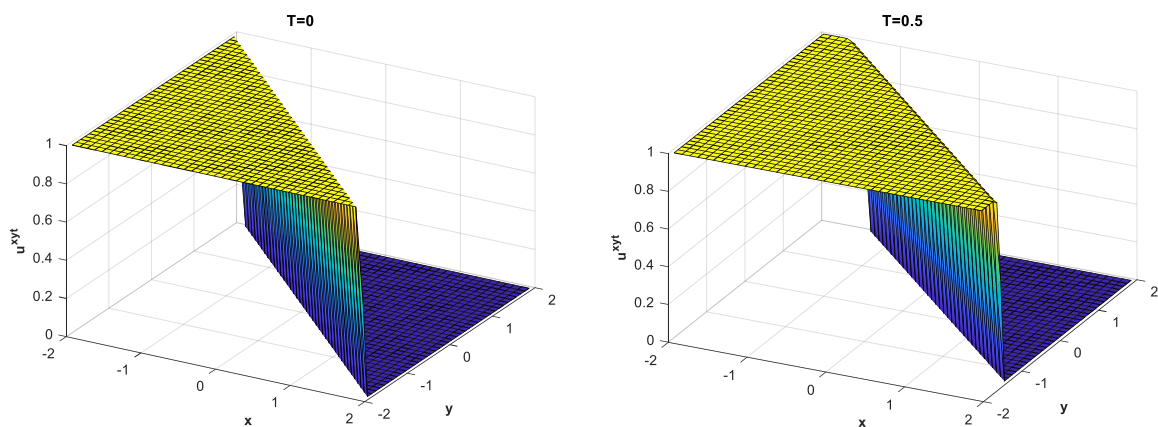
The third example focuses on a shock wave that propagates at a 45-degree angle to the node orientation. This two-dimensional problem serves as an extension of the previously described one-dimensional case, and the exact solution follows a similar pattern, which is represented as follows:

$$u(x, y, t) = \frac{1}{2} \left[1 - \tanh \left(\frac{xRe}{4} + \frac{yRe}{4} - \frac{tRe}{4} \right) \right] \quad (100)$$

and

$$v(x, y, t) = \frac{1}{2} \left[1 - \tanh \left(\frac{xRe}{4} + \frac{yRe}{4} - \frac{tRe}{4} \right) \right] \quad (101)$$

The domain of the problem is restricted to $[-2, 2] \times [-2, 2]$ and the initial and boundary conditions can be determined from the exact solution provided by Eq. (100) and Eq. (101).



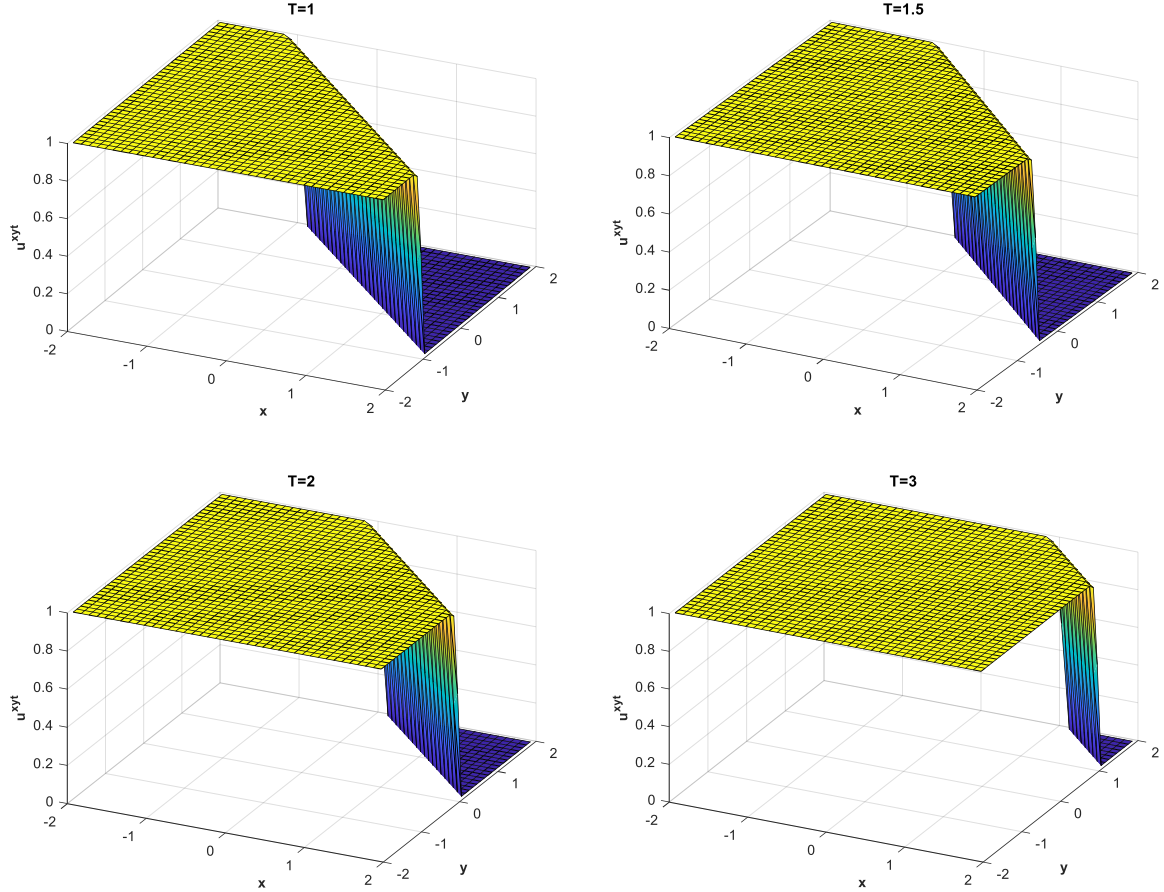


Figure 10 Numerical solution for **Example 3** using MCCNIM, illustrating the temporal evolution of the shock wave for $Re = 5000$, with a time step $\Delta t = 0.01$ and spatial resolution $\Delta x = 0.1$.

Figure 10 presents a 3D surface plot that visually captures the dynamic behavior of the propagating wave for the two-dimensional case at distinct time points ($T=0$, $T=0.5$, $T=1$, $T=1.5$, $T=2$, and $T=3$). These plots provide a clear depiction of the wave evolution over time. Notably, at a high Reynolds number of $Re = 5000$, the wavefront exhibits remarkable smoothness, even when computed on a very coarse grid ($\Delta x = 0.1$). This observation highlights the robustness and accuracy of the developed scheme, validating its effectiveness for solving two-dimensional problems. The progression of the shock wave shown in Figure 10 is further analyzed at each time point using 2D line plots, where the value of $x=0.7$ is held constant, as illustrated in Figure 11. These plots emphasize the comparison between the numerical and exact solutions. The numerical solution shows excellent agreement with the exact solution, even on coarse grids, despite the challenge of capturing a steep front propagating at an angle to the grid orientation. Notably, Figure 11 demonstrates the impressive performance of the

MCCNIM scheme, achieving a high degree of alignment with the exact solution at a high Reynolds number ($Re = 5000$) using a relatively coarse grid resolution of 40×40 .

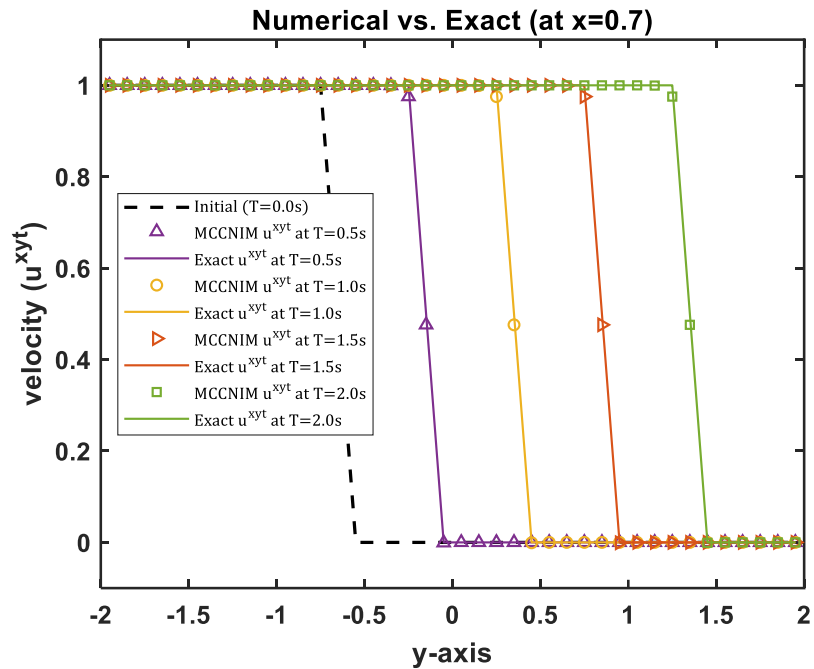
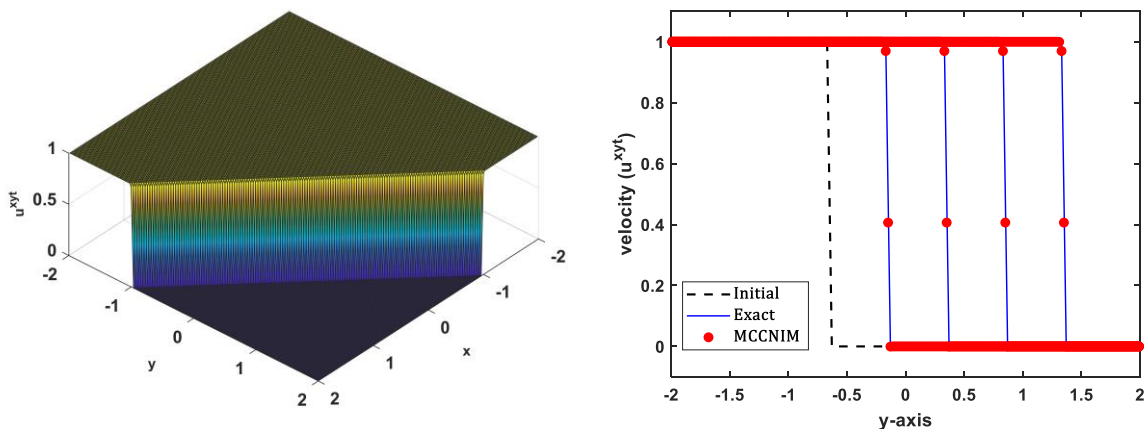


Figure 11 Comparison of numerical and exact velocity profiles (\bar{u}^{xyt}) for **Example 3** at $x = 0.7$, evaluated at various time points for $Re = 5000$, with a time step $\Delta t = 0.01$ and spatial resolution $\Delta x = 0.1$.

To further evaluate the efficacy of the developed scheme for a two-dimensional case at higher Reynolds numbers, we solved the problem for $Re = 40,000$, as illustrated in Figure 12. The numerical solution is compared with the exact solution, and it is evident from Figure 12 that the two solutions agree closely, underscoring the effectiveness of the proposed scheme for two-dimensional case.



(a) 3D surface plot at $T = 1$ sec

(b) 2D line plots

Figure 12 Numerical solution obtained using MCCNIM for $Re = 40,000$ (a) Surface plot illustrating the complete solution pattern at $T = 1$ second with the grid size $\Delta x = 0.02$ and time step $\Delta t = 0.005$. (b) Velocity profiles (\bar{u}^{xyt}) at $x = 0.7$, compared at four distinct time points ($T = 0.5, 1, 1.5,$ and 2 secs) with analytical solution.

It is important to highlight that this two-dimensional problem serves as an extension of the earlier one-dimensional case, for which we conducted a detailed error analysis. Given the favourable performance observed in the one-dimensional case using the MCCNIM scheme, it is reasonable to anticipate its superior performance in the two-dimensional context as well, surpassing other nodal schemes. Additionally, due to the lack of error data for NIM in existing literature for two-dimensional case, our comparison relies exclusively on evaluating the numerical solution against the exact solution. Notably, this comparison reveals a strong agreement between the numerical and exact solutions across a range of Reynolds numbers, from lower to higher values.

4 Conclusions

The developed MCCNIM is rigorously formulated for solving multidimensional Burgers' equations. Its effectiveness is initially evaluated by comparing RMS errors with the traditional NIM for the one-dimensional Burgers' equation. The results confirm the second-order accuracy of MCCNIM in both spatial and temporal domains. To further validate its performance, the scheme is extended to solve two-dimensional time-dependent coupled Burgers' equations. Classic benchmark problems with well-known analytical solutions are employed to demonstrate the scheme's accuracy and robustness in both one- and two-dimensional cases. Comparative analysis with traditional numerical schemes from existing literature highlights the ability of MCCNIM to efficiently and accurately address nonlinear problems. These findings establish a strong foundation for extending MCCNIM to more complex fluid dynamics problems, including applications to the Navier-Stokes equations.

References

- [1] D.L. Delp, J.M. Harriman, M.J. Stedwell, "A three-dimensional boiling water reactor simulator." FLARE, 1964. Scientific Report.
- [2] R.G. Steinke, A Coarse Nodal Method for Solving the Neutron Diffusion Equation, University of Michigan, 1973. PhD Thesis.

- [3] T.J. Burns, The Partial Current Balance Method: A Local Green's Function Technique for the Numerical Solution of Multidimensional Diffusion Problems, University of Illinois, 1975. PhD Thesis.
- [4] R.D. Lawrence, J.J. Dorning, A nodal green's function method for multidimensional neutron diffusion calculations, *Nuclear Science and Engineering* 76 (1980) 218–231. <https://doi.org/10.13182/NSE80-A19452>.
- [5] J.J. Dorning, Modern coarse-mesh methods-A development of the 70's, in: *Proc. Conf. Computational Methods in Nuclear Engineering*, American Nuclear Society, Williamsburg, VA, 1979.
- [6] J.P. Hennart, A general family of nodal schemes, *SIAM Journal on Scientific and Statistical Computing* 7 (1986) 264–287. <https://doi.org/10.1137/0907018>.
- [7] R.D. Lawrence, Progress in nodal methods for the solution of the neutron diffusion and transport equations, *Progress in Nuclear Energy* 17 (1986) 271–301.
- [8] M. Raj, N. Ahmed, S. Singh, Analytical nodal method for solution of neutron diffusion equation in polar coordinates, *Ann Nucl Energy* 165 (2022) 108659. <https://doi.org/10.1016/j.anucene.2021.108659>.
- [9] R.A. Shober, R.N. Sims, A.F. Henry, Two Nodal Methods for Solving Time-Dependent Group Diffusion Equations, *Nuclear Science and Engineering* 64 (1977) 582–592. <https://doi.org/10.13182/NSE77-A27392>.
- [10] R.M. Ferrer, Y.Y. Azmyt, Error analysis of the nodal integral method for solving the neutron diffusion equation in two-dimensional cartesian geometry, *Nuclear Science and Engineering* 162 (2009) 215–233. <https://doi.org/10.13182/NSE162-215>.
- [11] Y.Y. Azmy, A nodal integral approach to the numerical solution of partial differential equations, in: *Advances in Reactor Computations*, LaGrange Park, IL, 1983.
- [12] M. Raj, S. Singh, Solution of neutron diffusion equation in 2d polar (r,θ) coordinates using Nodal Integral Method, *Ann Nucl Energy* 105 (2017) 69–78. <https://doi.org/10.1016/j.anucene.2017.02.025>.
- [13] R.A. Shober, A nodal method for solving transient fewgroup neutron diffusion equations, Argonne National Laboratory, 1978. PhD Thesis.
- [14] Rizwan-Uddin, An improved coarse-mesh nodal integral method for partial differential equations, *Numer Methods Partial Differ Equ* 13 (1997) 113–145.
- [15] Rizwan-Uddin, A second-order space and time nodal method for the one-dimensional convection-diffusion equation, *Comput Fluids* 26 (1997) 233–247.

- [16] F. Wang, Rizwan-Uddin, A modified nodal scheme for the time-dependent, incompressible Navier–Stokes equations, *J Comput Phys* 187 (2003) 168–196. [https://doi.org/10.1016/S0021-9991\(03\)00093-7](https://doi.org/10.1016/S0021-9991(03)00093-7).
- [17] N. Ahmed, S. Singh, A modified cell-centered nodal integral scheme for the convection-diffusion equation, *J Comput Sci* 80 (2024) 102320. <https://doi.org/10.1016/j.jocs.2024.102320>.
- [18] N. Ahmed, G. Maurya, S. Singh, A novel cell-centered nodal integral method for the convection-diffusion equation, *Ann Nucl Energy* 189 (2023) 109858. <https://doi.org/10.1016/j.anucene.2023.109858>.
- [19] N. Ahmed, N. Kumar, S. Singh, Node averaged nodal integral method, in: 14th WCCM-ECCOMAS Congress, CIMNE, 2021. <https://doi.org/10.23967/wccm-eccomas.2020.219>.
- [20] O.A. Elnawawy, A.J. Valocchi, A.M. Ougouag, The cell analytical-numerical method for solution of the advection-dispersion equation: two-dimensional problems, *Water Resour Res* 26 (1990) 2705–2716. <https://doi.org/10.1029/WR026i011p02705>.
- [21] E.P.E. Michael, J. Dorning, Rizwan-Uddin, Studies on nodal integral methods for the convection-diffusion equation, *Nuclear Science and Engineering* 137 (2001) 380–399. <https://doi.org/10.13182/NSE137-380>.
- [22] Rizwan-Uddin, A second-order space and time nodal method for the one-dimensional convection-diffusion equation, *Comput Fluids* 26 (1997) 233–247.
- [23] Rizwan-Uddin, An improved coarse-mesh nodal integral method for partial differential equations, *Numer Methods Partial Differ Equ* 13 (1997) 113–145.
- [24] B.L. Wescott, Rizwan-uddin, An Efficient Formulation of the Modified Nodal Integral Method and Application to the Two-Dimensional Burgers' Equation, *Nuclear Science and Engineering* 139 (2001) 293–305. <https://doi.org/10.13182/NSE01-A2239>.

Appendix A

MCCNIM coefficients for 1D Burgers' equation

The coefficients for the averaged flux equations (i.e., Eq. (20) and Eq. (21)) are as follows:

$$A_{31} = \frac{2ae^{2aReu_{i,j}Re^2u_{i,j}^0}^2}{-1+e^{Reu_{i,j}}-2ae^{Reu_{i,j}Reu_{i,j}^{xt}}}$$

$$A_{32} = \frac{1-e^{Reu_{i,j}}+2ae^{Reu_{i,j}Reu_{i,j}^0}-2a^2e^{Reu_{i,j}Re^2u_{i,j}^0}^2}{u_{i,j}^{xt}(-1+e^{Reu_{i,j}}+2ae^{Reu_{i,j}Reu_{i,j}^0})}$$

$$A_{51} = \frac{2aRe^2u_{i,j}^0}^2}{-1+e^{Reu_{i,j}}-2aReu_{i,j}^0}$$

$$A_{52} = \frac{1-e^{Reu_{i,j}}+2aReu_{i,j}^0+2a^2Re^2u_{i,j}^0}^2}{u_{i,j}^0(-1+e^{Reu_{i,j}}-2aReu_{i,j}^0)}$$

The coefficients of the final set of algebraic equations (i.e., Eq. (35)-(37)) for the general interior node in one-dimensional Burgers' case are given as follows:

$$F_{31} = \frac{A_{32}(A_{51,i+1}-Reu_{i,j}^0)}{2aRe(A_{31}-A_{51,i+1})} + \frac{A_{52}(A_{31,i-1}-Reu_{i,j}^0)}{2aRe(A_{31,i-1}-A_{51})}$$

$$F_{32} = -\frac{A_{32,i-1}(A_{51}-Reu_{i,j}^0)}{2aRe(A_{31,i-1}-A_{51})}$$

$$F_{33} = -\frac{A_{52,i+1}(A_{31}-Reu_{i,j}^0)}{2aRe(A_{31}-A_{51,i+1})}$$

$$F_{34} = \frac{A_{31}(A_{51,i+1}-Reu_{i,j}^0)}{2aRe(A_{31,i-1}-A_{51})} + \frac{A_{51}(A_{31,i-1}-Reu_{i,j}^0)}{2aRe(A_{31,i-1}-A_{51})}$$

$$F_{35} = -\frac{A_{31,i-1}(A_{51}-Reu_{i,j}^0)}{2aRe(A_{31,i-1}-A_{51})}$$

$$F_{36} = -\frac{A_{51,i+1}(A_{31}-Reu_{i,j}^0)}{2aRe(A_{31}-A_{51,i+1})}$$

$$F_{51} = \frac{2\tau F_{31}}{1-2\tau F_{34}}; F_{52} = \frac{2\tau F_{32}}{1-2\tau F_{34}}; F_{53} = \frac{2\tau F_{33}}{1-2\tau F_{34}}; F_{54} = \frac{\tau}{1-2\tau F_{34}}; F_{55} = \frac{\tau}{1-2\tau F_{34}}$$

$$F_{56} = \frac{1}{1-2\tau F_{34}}; F_{57} = \frac{2\tau F_{35}}{1-2\tau F_{34}}; F_{58} = \frac{2\tau F_{36}}{1-2\tau F_{34}}$$

The coefficients of the final set of algebraic equations (i.e., Eq. (44) and Eq. (45)) for the right boundary (Dirichlet boundary) node in one-dimensional Burger's case are given as follows:

$$F_{31}^R = -\frac{A_{32}}{2aRe} + \frac{A_{52}(A_{31,i-1}-Reu_{i,j}^0)}{2aRe(A_{31,i-1}-A_{51})}$$

$$F_{32}^R = -\frac{A_{32,i-1}(A_{51}-Reu_{i,j}^0)}{2aRe(A_{31,i-1}-A_{51})}$$

$$F_{33}^R = 0$$

$$F_{34}^R = \frac{A_{31}}{2aRe} + \frac{A_{51}(A_{31,i-1}-Reu_{i,j}^0)}{2aRe(A_{31,i-1}-A_{51})}$$

$$F_{35}^R = -\frac{A_{31,i-1}(A_{51}-Reu_{i,j}^0)}{2aRe(A_{31,i-1}-A_{51})}$$

$$F_{36}^R = -\frac{(A_{31}-Reu_{i,j}^0)}{2aRe}$$

The coefficients, F_5^R 's retain the same form as those defined for the general node (F_5 's), with the key difference being that these coefficients now depend on F_3^R 's instead of F_3 . For instance, F_{51}^R is given by $F_{51}^R = \frac{2\tau F_{31}^R}{1-2\tau F_{34}^R}$. Similarly, expressions for the coefficients at the left boundary node can be derived following the same approach. Additionally, the coefficients corresponding to the Neumann boundary condition can be obtained in a comparable manner.

MCCNIM coefficients for 2D Burgers' equation

The coefficients for the two-dimensional Burgers' equation, as detailed in Section 2.2, are presented here for clarity. These include (A 's, B 's, F 's, G 's, L 's, M 's, N 's). Notably:

- The definitions of A 's and F 's remain identical to those in the one-dimensional case.
- The initial B 's coefficients, which are analogous to A 's, are given as follows:

$$B_{31} = \frac{2be^{Rev_{i,j}}Re^2v_{i,j}^0}{-1+e^{Rev_{i,j}-2be^{Rev_{i,j}}Rev_{i,j}^0}}$$

$$B_{32} = \frac{1 - e^{Rev_{i,j} + 2be^{Rev_{i,j} Rev_{i,j}^0} - 2b^2 e^{Rev_{i,j} Re^2 v_{i,j}^0}}}{v_{i,j}^0 (-1 + e^{Rev_{i,j} + 2be^{Rev_{i,j} Rev_{i,j}^0})}$$

$$B_{51} = \frac{2bRe^2 v_{i,j}^0}{-1 + e^{Rev_{i,j} - 2bRev_{i,j}^0}}$$

$$B_{52} = \frac{1 - e^{Rev_{i,j} + 2bRev_{i,j}^0 + 2b^2 Re^2 v_{i,j}^0}}{v_{i,j}^0 (-1 + e^{Rev_{i,j} - 2bRev_{i,j}^0})}$$

The coefficients of the final set of algebraic equations (i.e., Eq. (80)-(83)) for the two-dimensional Burgers' equation:

$$G_{31} = \frac{B_{32}(B_{51,j+1} - Rev_{i,j}^0)}{2bRe(B_{31} - B_{51,j+1})} + \frac{B_{52}(B_{31,j-1} - Rev_{i,j}^0)}{2bRe(B_{31,j-1} - B_{51})}$$

$$G_{32} = -\frac{B_{32,j-1}(B_{51} - Rev_{i,j}^0)}{2bRe(B_{31,j-1} - B_{51})}$$

$$G_{33} = -\frac{B_{52,j+1}(B_{31} - Rev_{i,j}^0)}{2bRe(B_{31} - B_{51,j+1})}$$

$$G_{34} = \frac{B_{31}(B_{51,j+1} - Rev_{i,j}^0)}{2bRe(B_{31,j-1} - B_{51})} + \frac{B_{51}(B_{31,j-1} - Rev_{i,j}^0)}{2bRe(B_{31,j-1} - B_{51})}$$

$$G_{35} = -\frac{B_{31,j-1}(B_{51} - Rev_{i,j}^0)}{2bRe(B_{31,j-1} - B_{51})}$$

$$G_{36} = -\frac{B_{51,j+1}(B_{31} - Rev_{i,j}^0)}{2bRe(B_{31} - B_{51,j+1})}$$

$$M_{51} = \frac{2\tau F_{31}}{1 + 2\tau F_{34} + 2\tau G_{34}}; \quad M_{52} = \frac{2\tau F_{32}}{1 + 2\tau F_{34} + 2\tau G_{34}}; \quad M_{53} = \frac{2\tau F_{33}}{1 + 2\tau F_{34} + 2\tau G_{34}};$$

$$M_{54} = \frac{2\tau F_{35}}{1 + 2\tau F_{34} + 2\tau G_{34}}; \quad M_{55} = \frac{2\tau F_{36}}{1 + 2\tau F_{34} + 2\tau G_{34}};$$

$$N_{51} = \frac{2\tau G_{31}}{1 + 2\tau F_{34} + 2\tau G_{34}}; \quad N_{52} = \frac{2\tau G_{32}}{1 + 2\tau F_{34} + 2\tau G_{34}}; \quad N_{53} = \frac{2\tau G_{33}}{1 + 2\tau F_{34} + 2\tau G_{34}};$$

$$N_{54} = \frac{2\tau G_{34}}{1 + 2\tau F_{34} + 2\tau G_{34}}; \quad N_{55} = \frac{2\tau G_{35}}{1 + 2\tau F_{34} + 2\tau G_{34}}$$

$$L_{51} = \frac{\tau}{1+2\tau F_{34}+2\tau G_{34}}; \quad L_{52} = \frac{\tau}{1+2\tau F_{34}+2\tau G_{34}}; \quad L_{53} = \frac{1}{1+2\tau F_{34}+2\tau G_{34}}; \quad L_{54} = \frac{2\tau}{1+2\tau F_{34}+2\tau G_{34}}$$

MCCNIM coefficients for node-averaged velocity in both 1D and 2D Burgers' equation

The coefficients for the equation node-averaged velocity $u_{i,j}^0$ given by Eq. (39) in the one-dimensional Burgers' case are expressed as follows:

$$F_{71} = \frac{A_{32,i-1}}{2(A_{31,i-1}-A_{51})}$$

$$F_{72} = \frac{A_{32}}{2(A_{31}-A_{51,i+1})} - \frac{A_{52}}{2(A_{31,i-1}-A_{51})}$$

$$F_{73} = -\frac{A_{52,i+1}}{2(A_{31}-A_{51,i+1})}$$

$$F_{74} = \frac{A_{31,i-1}}{2(A_{31,i-1}-A_{51})}$$

$$F_{75} = -\frac{A_{51}}{2(A_{31,i-1}-A_{51})} + \frac{A_{31}}{2(A_{31}-A_{51,i+1})}$$

$$F_{76} = -\frac{A_{51,i+1}}{2(A_{31}-A_{51,i+1})}$$

Similarly, the equation of the node-averaged velocities $u_{i,j,k}^0$ and $v_{i,j,k}^0$ given by Eq. (90) in the two-dimensional Burgers' case are expressed as follows:

$$G_{71} = \frac{B_{32,j-1}}{2(B_{31,j-1}-B_{51})}$$

$$G_{72} = \frac{B_{32}}{2(B_{31}-B_{51,j+1})} - \frac{B_{52}}{2(B_{31,j-1}-B_{51})}$$

$$G_{73} = -\frac{B_{52,j+1}}{2(B_{31}-B_{51,j+1})}$$

$$G_{74} = \frac{B_{31,j-1}}{2(B_{31,j-1}-B_{51})}$$

$$G_{75} = -\frac{B_{51}}{2(B_{31,j-1}-B_{51})} + \frac{B_{31}}{2(B_{31}-B_{51,j+1})}$$

$$G_{76} = -\frac{B_{51,j+1}}{2(B_{31}-B_{51,j+1})}$$

The coefficients of F_7 's in the two-dimensional Burger's equation will mirror those used in the one-dimensional Burger's equation.